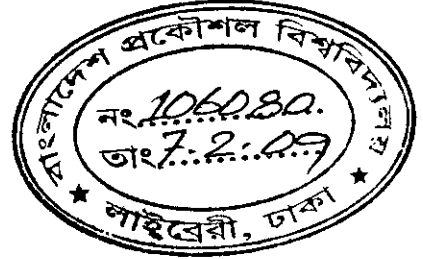


Full Band Simulation of Silicon Nanowire Field Effect Transistor



A thesis submitted to
the department of Electrical and Electronic Engineering
of
Bangladesh University of Engineering and Technology
in partial fulfillment of the requirement
for the degree of
MASTER OF SCIENCE IN ELECTRICAL AND ELECTRONIC ENGINEERING

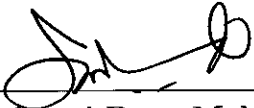
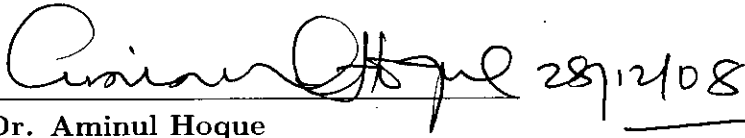
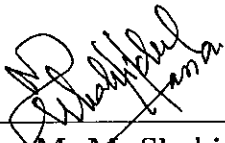

by
Redwan Noor Sajjad



DEPARTMENT OF ELECTRICAL AND ELECTRONIC ENGINEERING
BANGLADESH UNIVERSITY OF ENGINEERING AND TECHNOLOGY
2008

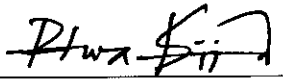
The thesis titled “ **Full Band Simulation of Silicon Nanowire Field Effect Transistor**” submitted by Redwan Noor Sajjad, Roll No.: 100606222P, Session: October 2006 has been accepted as satisfactory in partial fulfillment of the requirement for the degree of MASTER OF SCIENCE IN ELECTRICAL AND ELECTRONIC ENGINEERING on December 28, 2008.

BOARD OF EXAMINERS

1. 
_____ **Dr. Quazi Deen Mohd Khosru** **Chairman**
Professor (Supervisor)
Department of Electrical and Electronic Engineering
BUET, Dhaka-1000, Bangladesh.
2. 
_____ **Dr. Aminul Hoque** **Member**
Professor and Head (Ex-officio)
Department of Electrical and Electronic Engineering
BUET, Dhaka-1000, Bangladesh.
3. 
_____ **Dr. M. M. Shahidul Hassan** **Member**
Professor
Department of Electrical and Electronic Engineering
BUET, Dhaka-1000, Bangladesh.
4. 
_____ **Dr. Khairul Alam** **Member**
Assistant Professor (External)
Department of Electrical and Electronic Engineering
East West University, Mohakhali, Dhaka-1212, Bangladesh.

Declaration

I hereby declare that this thesis or any part of it has not been submitted elsewhere for the award of any degree or diploma.



(Redwan Noor Sajjad)

Contents

Declaration	ii
Acknowledgement	viii
Abstract	ix
1 Introduction	1
1.1 Literature Review	1
1.2 Objective of the Work	3
1.3 Organization of the thesis	3
2 Methodology	5
2.1 Generate Atomic Positions within a Nanowire	5
2.2 Building the Tight-Binding Hamiltonian	11
2.3 Retarded Green Function Algorithm for Charge Calculation	12
2.4 RGFA for Current Calculation	13
2.5 Poisson Solver	14
2.6 The Self Consistent Loop	15
2.7 Current Calculation Using Effective Mass Approximation	17
3 Results and Discussions	20
3.1 Electronic Properties of Silicon Nanowire	20
3.2 Effects of Cross-Sectional Shape on the Electronic Properties	28

3.3 I-V Response of the SiNWFET	35
4 Conclusions	41
4.1 Suggestions for Future Work	41
Appendix A Energy Integral Expressions	48
Appendix B Empirical Tight Binding Parameters	53
Appendix C Flow Chart of the Self Consistent Loop	55

List of Figures

Figure 2.1 Unit cell of a Silicon crystal.	5
Figure 2.2 Cross-sections of various shapes, (a) $\langle 100 \rangle$ and (b) $\langle 110 \rangle$ NW.	10
Figure 2.3 The device cross section used for simulation.	15
Figure 2.4 The initial guess of the potential distribution for $V_G = 0$.	17
Figure 3.1 The cross sections of (a) $\langle 100 \rangle$ and (b) $\langle 110 \rangle$ nanowires. The gray atoms are Silicon and the black atoms are hydrogen.	21
Figure 3.2 The band structure plots (E vs. k) of a $\langle 100 \rangle$ wire of cross section $3.295 \text{ nm} \times 3.295 \text{ nm}$.	22
Figure 3.3 The band structure plots (E vs. k) of a $\langle 110 \rangle$ wire of cross section $3.508 \text{ nm} \times 3.508 \text{ nm}$.	23
Figure 3.4 The band gap versus wire dimension for the (a) $\langle 100 \rangle$ and (b) $\langle 110 \rangle$ wires. The solid lines are calculated from the $sp^3d^5s^*$ orbital basis and the dashed lines are fitting to analytic expression.	25
Figure 3.5 The electron effective masses $m_{\Delta 1}$ and $m_{\Delta 2}$ versus wire dimension for the $\langle 100 \rangle$ wires. The solid lines are calculated from the $sp^3d^5s^*$ orbital basis and the dotted lines are fitting to analytic expression.	27

Figure 3.6 The electron effective masses m_1 and m_2 versus wire dimension for the $\langle 110 \rangle$ wires. The definitions of m_1 and m_2 are given in the text. The solid lines are calculated from the $sp^3d^5s^*$ orbital basis and the dotted lines are fitting to analytic expression. Figure (c) is the E-k relations near the Γ point for two different wires to explain the behavior of m_1 with wire dimension.	29
Figure 3.7 The bandstructure of $\langle 100 \rangle$ SiNWs with (a) square, (b) Circular, (c) Triangular cross-section	30
Figure 3.8 Bandgap variation with (a) dimension, (b) cross-section area.	30
Figure 3.9 Effect of wire cross-section area on Δ_4 and Δ_2 conduction band valleys, (a) Variation of fourth highest conduction band energy at Δ_4 valley taking the lowest energy as reference, (b) Splitting of Δ_4 and Δ_2 valleys.	31
Figure 3.10 Effect of wire area on the splitting of the three highest valence bands taking the highest valence band Ev_1 as reference, (a) The energies Ev_2 and (b) Ev_3 with respect to Ev_1 .	32
Figure 3.11 Electron effective mass for $\langle 100 \rangle$ wire at (a) Δ_4 valley (b) Δ_2 valley versus area.	33
Figure 3.12 Variation of electron effective mass with area for $\langle 110 \rangle$ wire, (a) m_1 and (b) m_2 . The definitions of m_1 and m_2 are given in the text.	34
Figure 3.13 Variation of hole effective mass with area for $\langle 100 \rangle$ wire.	35
Figure 3.14 Simulated I_D versus V_{GS} plots. The solid lines are full band calculation and the dashed lines are calculated from nanowire confined effective mass model. The nanowire is $\langle 110 \rangle$ with cross section of $0.82 \text{ nm} \times 0.82 \text{ nm}$.	36

- Figure 3.15 The conduction bands superimposed on the energy distribution of current in both (a) off-state and (b) on-state. The solid lines are full band calculation and the dashed lines are calculated from nanowire confined effective mass model. 37
- Figure 3.16 The gate capacitance, the transconductance, the switching delay, and the unity current gain frequency versus gate bias. The drain to source bias is fixed to 0.5 V. 38
- Figure 3.17 Simulated I_D versus V_{GS} plots. The solid lines are full band calculation and the dotted lines are calculated from nanowire confined effective mass model. The nanowire is $\langle 110 \rangle$ with cross section of $1.2 \text{ nm} \times 1.2 \text{ nm}$. 39

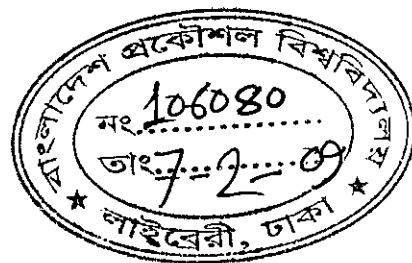
Acknowledgement

I wish to convey my heartiest gratitude and profound respect to my supervisor Dr. Quazi Deen Mohd Khosru, Professor, Department of Electrical and Electronic Engineering (EEE), Bangladesh University of Engineering and Technology (BUET), Dhaka, for his continuous guidance, suggestions and wholehearted supervision throughout the progress of this work, without which this thesis would never have been materialized.

I want to thank Dr. Aminul Hoque, Professor and Head, Dept. of EEE, BUET for taking necessary measures to provide modern computers in the simulation laboratory where the entire simulation work was done. I want to thank my friends and colleagues in the department of EEE, BUET for engaging in fruitful discussions and many others, who were directly or indirectly related to this work, for their support and encouragement.

Abstract

Full band simulation studies are performed for Silicon nanowires using $sp^3d^5s^*$ orbital basis tight-binding approach. The electronic properties of Silicon nanowires have been studied for different growth directions, shape and size of the cross-section. Then the I-V response are calculated for an n-channel Silicon nanowire transistor of wire cross section $0.82\text{ nm}\times 0.82\text{ nm}$ and $1.2\text{ nm}\times 1.2\text{ nm}$ using the same basis. The smaller device has the tunneling and thermal components of current in both off and on states. The intrinsic switching delay is in the fraction of picosecond and the unity current gain frequency is in Tera Hertz range. The device has an on/off current ratio of 10^7 and near ideal subthreshold slope. Simulation is also performed using nanowire confined effective masses and is compared against the full band calculation. The full band and effective mass I-V characteristics of $1.2\text{ nm}\times 1.2\text{ nm}$ wire show very good agreement. However, relatively larger mismatch is observed for the $0.82\text{ nm}\times 0.82\text{ nm}$ wire, especially at the lower gate biases. This is because the current has both the thermal and tunneling components, and the nanowire effective mass model overestimates the tunneling current. This overestimation is relatively larger for thinner wires. The thermal component of current is same in both the nanowire effective mass and full band models. To facilitate simulation using nanowire effective mass model, we calculate the band structure using $sp^3d^5s^*$ atomic orbital basis, extract the band gap and electron effective masses, and fit them to analytic expression. Calculations are performed for nanowires grown in $\langle 100 \rangle$ and $\langle 110 \rangle$ directions.



Chapter 1

Introduction

There has been aggressive downscaling of conventional transistors in the past few years by reducing gate length, oxide thickness and channel depth. Performance degradation takes place due to this scaling including short channel effects, reduced electron mobility and weakened gate control. For future nanotechnology, novel materials such as nanowires (NW) can be useful building blocks because of their superior characteristics. They have attracted significant attentions [1, 2, 3, 4, 5, 6], because their electronic properties can be controlled in a predictable manner and they are compatible with the CMOS processes. Controlled growth of Silicon nanowires (SiNWs) down to 3 nm diameter [7], their applications as Field Effect Transistors (FETs) [1, 2, 5, 8], logic gates [9], and sensors [10] have been demonstrated. As the nanowires' dimension is in the nanometer regime, effects like tunneling and quantum confinement play dominant role. To understand device physics and to assess the performance simulation work is important.

1.1 Literature Review

Atomic orbital basis has been used to study electronic properties of SiNWs at material level [11, 12, 13, 14, 15] and also using first principle calculations. The bulk crystal symmetry is not preserved in SiNWs due to quantum confinement in the transverse directions, and therefore, the bulk effective mass approximation

fails for nanowires of smaller diameter [11]. The validity of bulk effective mass approximation has been investigated at device level using ballistic top of the barrier model [16] that ignores the tunneling current. For this, Wang *et al.* [16] have calculated the band structure and nanowire confined masses using $sp^3d^5s^*$ tight binding orbital basis. The Schrodinger's equation is then solved in continuum basis using both the bulk and nanowire masses. According to their study, the bulk effective mass approximation overestimates the threshold voltage for wire width < 3 nm and the on current for wire width < 5 nm. Nehari *et al.* [17] have extracted the subband position and transport effective masses from tight binding calculations. With these as the input parameters, they have solved Schrodinger's equation and have calculated current using mode space approach. Their study shows that the bulk effective mass overestimates the on/off current ratio for wire width < 3 nm, underestimates the tunneling current, and overestimates the thermal current. Gnani *et al.* [18] have investigated the effects of nonparabolic band structure on the electrical characteristics of Silicon Nanowire Field Effect Transistors (SiNWFETs) by expanding the dispersion relation in power series up to third order.

The simulations used so far to calculate the current-voltage characteristics use either bulk effective masses or nanowire confined effective masses. We find that Luisier *et al.* [19, 20] have performed full band I-V calculations, and very recently Boykin *et al.* [21] have developed an optimized renormalization method for efficient calculation of multiband transmission. The full band current calculation is very costly. The bulk effective mass approximation fails for nanowires of width < 5 nm. The nanowire confined effective mass model requires the atomistic calculation of band structure and extraction of effective masses. Moreover, the accuracy of nanowire confined effective mass model against the full band calculations should be verified. Recently Marconcini *et al.* [22] have compared the nanowire effective mass I-V with the full band calculations. Their full band I-V has been extracted

from [19]. In this paper, we perform full band ($sp^3d^5s^*$ orbital basis) simulation study of Silicon nanowire transistors, evaluate the performance metrics, calculate the band structure, extract the band gap and nanowire confined effective masses and fit them to analytic expression, and compare the I-V calculated from the nanowire effective mass model against the full band calculation. The focus is on the n-channel transistors for $\langle 100 \rangle$ and $\langle 110 \rangle$ grown nanowires. The band gap and the electron effective masses are found to fit the analytic expression $A_1 + A_2/W$, where A_1 and A_2 are fitting parameters and W is the nanowire width in nanometer. The current has both the tunneling and the thermal components. The nanowire effective mass model overestimates the tunneling component of current and this overestimation is relatively larger for thinner wires. The simulated I-V characteristics from both the parameterized effective mass model and the full band model closely match for wire dimension of 1.2 nm. The device has small capacitance in the atto Farad range. The intrinsic switching delay is in the fraction of picosecond and the intrinsic unity current gain frequency is in tera Hertz range.

1.2 Objective of the Work

The objectives of the work and possible outcomes are:

- To generate the atomic positions of a Silicon nanowire grown in any arbitrary direction.

- To show band structure for the grown nanowire using $sp^3d^5s^*$ tight binding orbital basis.

- To find the I-V characteristics of SiNWFET built from $\langle 110 \rangle$ oriented small diameter nanowire.

1.3 Organization of the thesis

The second chapter describes how the nanowire was grown and the tight-binding hamiltonian was built. We utilized Recursive Green Functions algorithm to get

charge density and calculate current from the converged potential profile. The poisson equation was solved in 2-D cylindrical co-ordinates. The second chapter also explains how the self-consistent loop was formed and how to calculate I-V characteristics from both full band and effective mass model. The third chapter discusses the results of the thesis. Then we conclude and make suggestions for future work in the forth chapter.

Chapter 2

Methodology

2.1 Generate Atomic Positions within a Nanowire

To build the tight-binding hamiltonian we need to know the atomic positions of individual atoms in the Silicon nanowire.

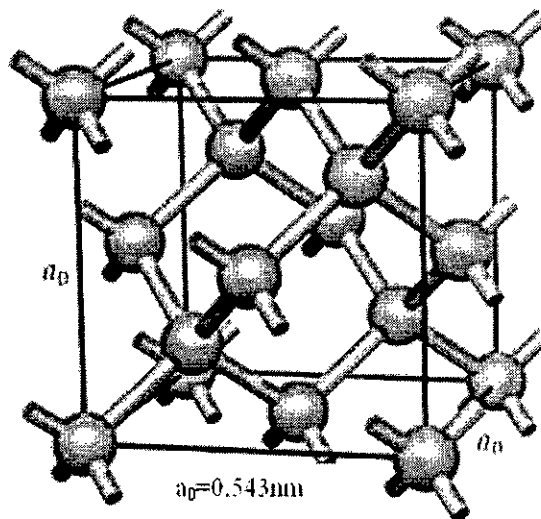


Figure 2.1: Unit cell of a Silicon crystal.

A mathematical model is developed to generate the atomic positions of a nanowire given the following parameters

- Crystallographic orientation
- Nanowire cross-section in nanometer square
- Shape of cross-section

The nanowire growth direction is symbolized as \vec{C}_1 which can be $\langle 100 \rangle$, $\langle 110 \rangle$, $\langle 111 \rangle$ etc. The model can generate a square nanowire. The Matlab program is then modified to produce nanowire of different cross-sectional shapes (e.g. circular, triangular, hexagonal, pentagonal and octagonal). The electronic properties depend heavily on crystal orientation and dimension. They also differ for different cross-sectional shapes. To grow a nanowire of the desired shape, a square nanowire is grown first, then the outer atoms are eliminated to form the desired shape.

Algorithm to Grow Nanowire:

The three basis vectors of FCC crystal

$$\vec{a}_1 = \frac{1}{2} \begin{pmatrix} 1 \\ 1 \\ 0 \end{pmatrix} \quad (2.1)$$

$$\vec{a}_2 = \frac{1}{2} \begin{pmatrix} 0 \\ 1 \\ 1 \end{pmatrix} \quad (2.2)$$

$$\vec{a}_3 = \frac{1}{2} \begin{pmatrix} 1 \\ 0 \\ 1 \end{pmatrix} \quad (2.3)$$

Therefore co-ordinates of anions can be obtained from

$$\vec{R}_i = n_1 \vec{a}_1 + n_2 \vec{a}_2 + n_3 \vec{a}_3 \quad (2.4)$$

While defining the crystal orientation \vec{C}_1 , the other two directions \vec{C}_2 and \vec{C}_3 are also defined such that \vec{C}_1 , \vec{C}_2 and \vec{C}_3 are mutually orthogonal.

• Step 1- Finding $\vec{R}_a, \vec{R}_b, \vec{R}_c$:

We need to find three atomic positions in the \vec{C}_1, \vec{C}_2 and \vec{C}_3 directions such that they are the first neighbors of the reference (0,0,0) atom in those directions. So now define these vectors $\vec{R}_a, \vec{R}_b, \vec{R}_c$ that are corresponding to those atomic positions

$$\vec{R}_a = (\text{someconstant}(sc))\vec{C}_1 \quad (2.5)$$

$$\vec{R}_b = (sc)\vec{C}_2 \quad (2.6)$$

$$\vec{R}_c = (sc)\vec{C}_3 \quad (2.7)$$

As $\vec{R}_a, \vec{R}_b, \vec{R}_c$ point to atomic positions they follow Equation 2.4

Let us calculate \vec{R}_a -

$$n_1a_1(x) + n_2a_2(x) + n_3a_3(x) = R_a(x) \quad (2.8)$$

$$n_1a_1(y) + n_2a_2(y) + n_3a_3(y) = R_a(y) \quad (2.9)$$

$$n_1a_1(z) + n_2a_2(z) + n_3a_3(z) = R_a(z) \quad (2.10)$$

$$\begin{pmatrix} a_1(x) & a_2(x) & a_3(x) \\ a_1(y) & a_2(y) & a_3(y) \\ a_1(z) & a_2(z) & a_3(z) \end{pmatrix} \begin{pmatrix} n_1 \\ n_2 \\ n_3 \end{pmatrix} = \begin{pmatrix} R_a(x) \\ R_a(y) \\ R_a(z) \end{pmatrix} \quad (2.11)$$

$$[a][n] = (sc)[C_1] \quad (2.12)$$

$$[a][n/sc] = [C_1] \quad (2.13)$$

$$[n/sc] = [a]^{-1}[C_1] \quad (2.14)$$

Solving Equation 2.14 will give the values of n_1, n_2, n_3 divided by a common denominator (or multiplied by a common factor). Dividing the result by the GCD

of the three numbers will give n_1, n_2 and n_3 . Similarly \vec{R}_b and \vec{R}_c are found.

•Step 2 - Generation of atomic co-ordinates in the volume spanned by the vectors $\vec{R}_a, \vec{R}_b, \vec{R}_c$:

The volume spanned by $\vec{R}_a, \vec{R}_b, \vec{R}_c$ has eight corners. The co-ordinates of those corners are

$$\begin{aligned} co - or_1 &= (0, 0, 0) \\ co - or_2 &= \vec{R}_a \\ co - or_3 &= \vec{R}_b \\ co - or_4 &= \vec{R}_c \\ co - or_5 &= \vec{R}_a + \vec{R}_b \\ co - or_6 &= \vec{R}_b + \vec{R}_c \\ co - or_7 &= \vec{R}_c + \vec{R}_a \\ co - or_8 &= \vec{R}_a + \vec{R}_b + \vec{R}_c \end{aligned}$$

All these co-ordinates correspond to atomic positions within the crystal and therefore follow Equation 2.4. Now solving Equation 2.14 with co-ordinates as the right hand sides will give 8 different values of n_1, n_2, n_3 . To get the atoms within the volume, we need to pick up the lowest and highest values of n_1, n_2, n_3 and vary each value of n_1, n_2, n_3 within the limit to get an atomic position and check whether the atom falls within the volume or not. For a particular set of n_1, n_2, n_3 ,

$$n_a \vec{R}_a + n_b \vec{R}_b + n_c \vec{R}_c = n_1 \vec{a}_1 + n_2 \vec{a}_2 + n_3 \vec{a}_3 = co\vec{or} \quad (2.15)$$

$$\begin{pmatrix} R_a(x) & R_b(x) & R_c(x) \\ R_a(y) & R_b(y) & R_c(y) \\ R_a(z) & R_b(z) & R_c(z) \end{pmatrix} \begin{pmatrix} n_a \\ n_b \\ n_c \end{pmatrix} = \begin{pmatrix} coor(x) \\ coor(y) \\ coor(z) \end{pmatrix} \quad (2.16)$$

$$[R][n] = [coor] \quad (2.17)$$

$$[n] = [R]^{-1}[coor] \quad (2.18)$$

if each of n_a, n_b, n_c is less than one, only then the $c\vec{o}r$ corresponds to an atom within the volume/unit cell. The co-ordinate will give the position of an anion. To get the corresponding cation, we need to do the following operation

$$c\vec{a}t\vec{i}o\vec{n} = a\vec{n}\vec{i}o\vec{n} + v\vec{e}c \quad (2.19)$$

where,

$$v\vec{e}c = \frac{1}{4} \begin{pmatrix} 1 \\ 1 \\ 1 \end{pmatrix} \quad (2.20)$$

•**Step 3 - Repeating the unit cell:**

Once the unit cell is formed, it is repeated along R_b and R_c directions until the desired cross-sectional area is achieved. This final set of co-ordinates is called super cell. The nanowire is a one-dimensional device and it is assumed to be infinite in the growth direction (R_a). So the super cell is repeated along R_a only for once. It will help us to construct the bandstructure of the nanowire according to. Finally hydrogen atoms are added at the open bonds at the wire boundaries. The Si-Si bond length is $2.35A^0$ and Si-H bond length is $1.49A^0$. The bond angle is the same on both occasions.

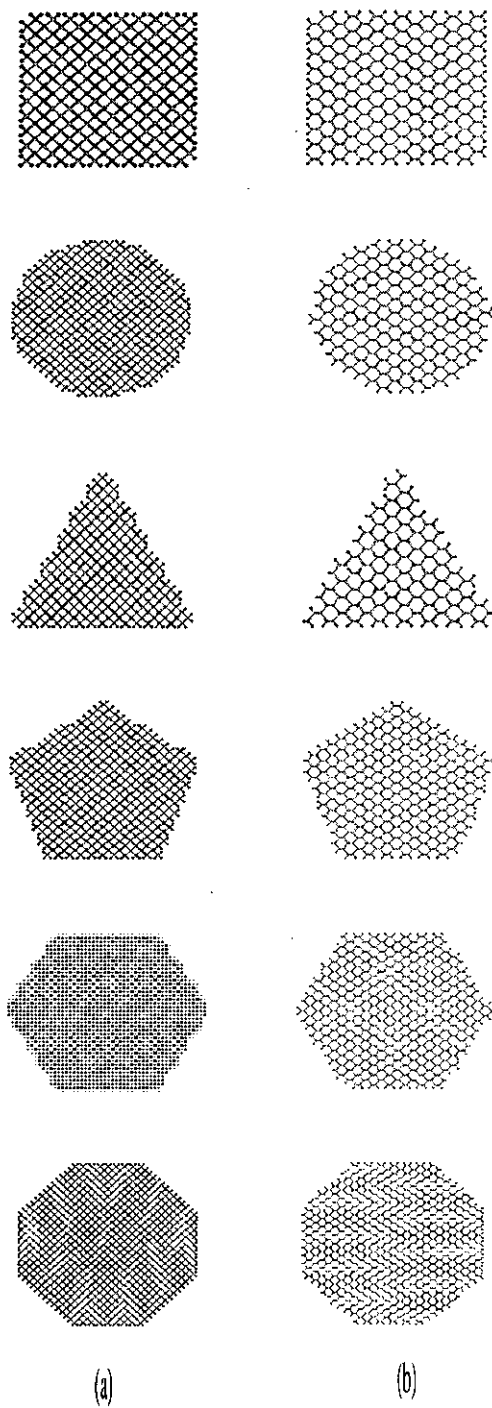


Figure 2.2: Cross-sections of various shapes, (a) $\langle 100 \rangle$ and (b) $\langle 110 \rangle$ NW.

2.2 Building the Tight-Binding Hamiltonian

The basis of the Hamiltonian is $sp^3d^5s^*$ and if the system contains for example, 2 atoms the hamiltonian will be a 20×20 matrix, each of the element of the matrix signifies the interaction between the orbitals. When two orbitals overlaps, the type of bond will be π , σ or/and δ depending on the type of orbitals involved. If one of the orbitals is s or s^* then only σ bond is possible.

In order to illustrate how the individual matrix element is calculate we can consider two examples. First, let us assume the two orbitals involved are both s orbitals. In this case the interaction element will be just equal to $V_{ss\sigma}$ which is the coupling energy between s orbitals and called orbital parameter. Although these parameters are tuned to produce bulk Silicon behavior we can still assume then can work very well for nanowires having dimension $>0.5\text{nm}$. If one orbital is changed to p orbital, then the expression will be $\langle \phi | \hat{H} | \phi \rangle = t(V_{sp\sigma})$. For band structure calculation, the Hamiltonian is created from

$$H(k_x) = H_0(k_x) + t_{01}e^{ik_x\Delta x} + t_{10}e^{-ik_x\Delta x}. \quad (2.21)$$

Here k_x is the one dimensional (1D) wave vector and Δx is the distance between the last layer of a unit cell and the first layer of the next unit cell. The matrix elements of $H_0(k_x)$ are created from

$$H_0(i, j) = \langle \phi_{i,n} | \hat{H} | \phi_{j,m} \rangle e^{ik_x(x_m - x_n)}, \quad (2.22)$$

and those of t_{01} are created from

$$t_{01}(p, q) = \langle \phi_{p,u} | \hat{H} | \phi_{q,v} \rangle. \quad (2.23)$$

Here n and m label the atoms in a unit cell, and u and v label the atoms between adjacent unit cells. The basis, ϕ , is the $sp^3d^5s^*$ atomic orbitals and $\phi_{j,m}$ is the j^{th} orbital of the m^{th} atom. The Hamiltonian is created under tight binding approximation. The energy integral expressions¹, $\langle \phi_{i,n} | \hat{H} | \phi_{j,m} \rangle$ and $\langle \phi_{p,u} | \hat{H} | \phi_{q,v} \rangle$,

¹A complete list of energy integral expressions and orbital parameters are provided in Appendix A and B

are taken from Slater [23], and the orbital parameters are taken from Boykin [24] and Zheng [11]. Spin-orbit coupling is not considered in this study. The band structure is obtained by calculating the eigen energies of $H(k_x)$ defined in Equation (2.21).

2.3 Retarded Green Function Algorithm for Charge Calculation

Non-equilibrium Green functions with empirical and atomistic Hamiltonians have been used over a decade with great success in quantum device simulation for both Silicon devices. The Recursive Green Function Algorithm (RGFA) is the most efficient algorithm known to solve the Green function equations. In the following section, we discuss briefly the RGFA.

Recursive Green function algorithm (RGFA) [25, 26] is used to solve nonequilibrium Green's function equations for charge density calculation. The charge density at each orbital of an atomic layer L is calculated from

$$\rho_L = (2q) \int \frac{dE}{2\pi} \text{diag}\{f_S A_{L,L}^L + f_D A_{L,L}^R\}. \quad (2.24)$$

$$\rho_L = (2q) \int \frac{dE}{2\pi} \text{diag}\{f_S A_{L,L}^L + f_D [A_{L,L} - A_{L,L}^L]\}. \quad (2.25)$$

Here f_S and f_D are the source and drain Fermi functions, respectively, and $A_{L,L}^L$, $A_{L,L}^R$ and $A_{L,L}$ are the left-connected, right-connected and full spectral functions, respectively, of the L^{th} atomic layer. $A_{L,L}^L$ and $A_{L,L}$ are full $N_{orb} \times N_{orb}$ matrices, where N_{orb} is the number of orbital in an atomic layer, and ρ_L is an $N_{orb} \times 1$ vector formed by taking the diagonal elements of the matrix on the right hand side of Equation (2.25). The left connected spectral function, the right connected spectral function and the full spectral function are calculated from [25, 27]

$$A_{L,L}^L = G_{L,1} \Gamma_{1,1}^L G_{L,1}^\dagger \quad (2.26)$$

$$A_{L,L}^R = G_{L,N} \Gamma_{N,L}^R G_{L,N}^\dagger \quad (2.27)$$

$$A_{L,L} = i(G_{L,L} - G_{L,L}^\dagger), \quad (2.28)$$

$$\Gamma_{1,1}^L = i(\Sigma_1 - \Sigma_1^\dagger) \quad (2.29)$$

$$\Gamma_{N,L}^R = i(\Sigma_2 - \Sigma_2^\dagger) \quad (2.30)$$

the retarded Green function is defined as

$$G = [EI - H_D - U - \Sigma_1 - \Sigma_2]^{-1} \quad (2.31)$$

Here H_D is the Hamiltonian. The self energies can be found from

$$\Sigma_1 = t_{10}g_{00}t_{01} \quad (2.32)$$

$$\Sigma_2 = t_{N,N+1}g_{N+1,N+1}t_{N+1,N} \quad (2.33)$$

The algorithm of Reference [28] is used to calculate surface green function g . The charge density obtained from Equation (2.25) at each atomic layer is interpolated to the Poisson's grids on that layer. Charge density is non-zero in Silicon nanowire only.

2.4 RGFA for Current Calculation

The coherent current can be calculated from one of the following

$$\begin{aligned} I &= \frac{2e}{h} \int dE \operatorname{tr} [\Gamma_{11} (A_{1,1} - G_{1,1}\Gamma_{1,1}G_{1,1}^\dagger)] (f^S - f^D) \text{ or} \\ I &= \frac{2e}{h} \int dE \operatorname{tr} [\Gamma_{11}G_{1,N}\Gamma_{N,N}G_{N,1}^\dagger] (f^S - f^D), \end{aligned} \quad (2.34)$$

where $A_{i,i} = i(G_{i,i} - G_{i,i}^\dagger)$ is the full spectral function. Therefore, we need the first column block and the diagonal block of retarded Green's function for electron density calculation and only the (1, 1) or (1, N) block for transmission calculation.

2.5 Poisson Solver

The potential distribution in poisson grid points is obtained from Poisson's equation in cylindrical coordinates.

Unit vectors

$$\hat{r} = (\cos\theta)\hat{x} + (\sin\theta)\hat{y} + (0)\hat{z} \quad (2.35)$$

$$\hat{\phi} = (-\sin\theta)\hat{x} + (\cos\theta)\hat{y} + (0)\hat{z} \quad (2.36)$$

$$\hat{z} = (0)\hat{x} + (0)\hat{y} + (1)\hat{z} \quad (2.37)$$

and

$$\hat{r} \cdot \hat{r} = \hat{\phi} \cdot \hat{\phi} = \hat{z} \cdot \hat{z} = 1 \quad (2.38)$$

$$\hat{r} \cdot \hat{\phi} = \hat{\phi} \cdot \hat{z} = \hat{z} \cdot \hat{r} = 0 \quad (2.39)$$

Derivative of unit vectors

All zero except

$$\frac{\partial \hat{\phi}}{\partial \phi} = -\hat{r} \quad (2.40)$$

$$\frac{\partial \hat{r}}{\partial \phi} = \hat{\phi} \quad (2.41)$$

Gradient

$$\nabla = \hat{r} \frac{\partial}{\partial r} + \hat{\phi} \frac{1}{r} \frac{\partial}{\partial \phi} + \hat{z} \frac{\partial}{\partial z} \quad (2.42)$$

Poisson equation (2D)

$$\nabla \cdot (\epsilon \nabla V) = -\rho \quad (2.43)$$

$$\left(\hat{r} \frac{\partial}{\partial r} + \hat{\phi} \frac{1}{r} \frac{\partial}{\partial \phi} + \hat{z} \frac{\partial}{\partial z} \right) \cdot \left[\epsilon \hat{r} \frac{\partial V}{\partial r} + \epsilon \hat{z} \frac{\partial V}{\partial z} \right] = -\rho \quad (2.44)$$

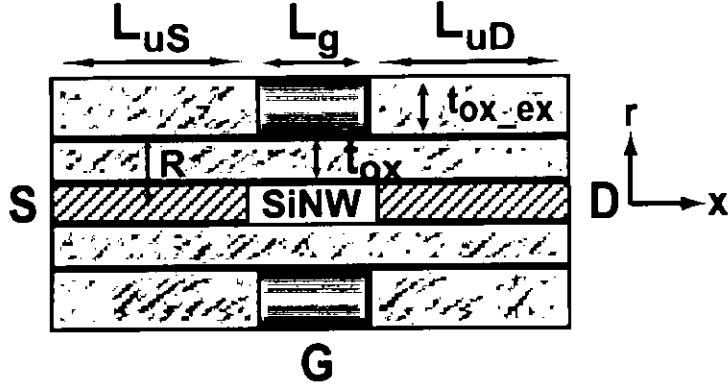


Figure 2.3: The device cross section used for simulation.

$$\epsilon \frac{\partial^2 V}{\partial r^2} + \frac{\partial V}{\partial r} \frac{\partial \epsilon}{\partial r} + \frac{1}{r} \epsilon \frac{\partial V}{\partial r} + \frac{\partial V}{\partial z} \frac{\partial \epsilon}{\partial z} + \epsilon \frac{\partial^2 V}{\partial z^2} = -\rho \quad (2.45)$$

$$\epsilon \left[\frac{\partial^2 V}{\partial r^2} + \frac{1}{r} \frac{\partial V}{\partial r} + \frac{\partial^2 V}{\partial z^2} \right] + \frac{\partial V}{\partial r} \frac{\partial \epsilon}{\partial r} + \frac{\partial V}{\partial z} \frac{\partial \epsilon}{\partial z} = -\rho \quad (2.46)$$

$$\frac{\partial^2 V}{\partial r^2} + \frac{\partial^2 V}{\partial z^2} + \left(\frac{1}{r} + \frac{1}{\epsilon} \frac{\partial \epsilon}{\partial r} \right) \frac{\partial V}{\partial r} + \frac{1}{\epsilon} \frac{\partial \epsilon}{\partial z} \frac{\partial V}{\partial z} = -\frac{\rho}{\epsilon} \quad (2.47)$$

here

$$\epsilon = \epsilon_0 \epsilon_r \quad (2.48)$$

where $\epsilon = \epsilon_0 \epsilon_r$ is the dielectric constant, V is the 2D potential and ρ is the 3D charge density, which is non-zero in Silicon nanowire only. The 2D Poisson's equation has been solved before for electrostatics of a gate-all-around Silicon nanowire transistor [29]. Poisson kernel is created by discretizing Equation (2.47) using finite difference.

2.6 The Self Consistent Loop

The cross section of the gate-all-around device used in our simulation is shown in Figure 2.3. The Silicon nanowire channel has a square cross section of $0.82 \text{ nm} \times 0.82 \text{ nm}$. We simulate 130 unit cells that is corresponding to the nanowire

length of 50 nm. The gate length, L_g , is 10 nm and the gate oxide thickness, t_{ox} , is 2 nm. The nanowire under the gate region (channel) is undoped and the doped source and drain extension, L_{uS} and L_{uD} , is 20 nm each. The uniform source-drain doping concentration of $2 \times 10^{20} \text{ cm}^{-3}$ is assumed. The gate oxide is SiO_2 with dielectric constant of 3.9. The channel has a band gap of 2.88 eV. For decent values of drain current, the gate metal-semiconductor work function difference, ϕ_{ms} , of 1.0 eV is used so that the zero gate bias potential barrier in the channel becomes approximately equal to the supply voltage. The simulation model uses a self-consistent solution between two dimensional (2D) electrostatics and three dimensional (3D) charge density.

With gate voltage set to a particular value, we assume an initial guess of orbital voltages. The orbital at the source region is assumed to have a voltage at E_f and those at the drain region have $E_f - V_D$. For gate region, the voltage is assumed as $E_f + E_g/2 - \phi_{ms}$ and ϕ_{ms} is set to 1.0 eV to reduce the barrier height and get a considerable amount of current. The initial guess of the potential distribution will look like in Figure 2.4. RGFA will provide the charge density at each orbital. The total charge of a particular atomic site is then calculated as the sum of all the orbital charges divided by the volume of an atom. Then the charge density at each atom is interpolated to find the density at poisson grid points.

Poisson equation is then solved to get potential distribution from the calculated charge density at poisson grid points using standard Newton-Raphson method with Anderson mixing [30] to accelerate convergence. Dirichlet boundary condition is used on the gate metal. There the potential is fixed to $V_{GS} - \Phi_G/q$, where Φ_G is the gate metal work function. Von Neumann boundary conditions are used along the exposed surface of the dielectric and at the doped source and drain contacts. There, the normal component of electric field is set to zero. The axial grids are taken at each atomic layer position. Potential obtained from Poisson solver at each atomic layer is interpolated to the atomic sites of that layer. And the orbitals are

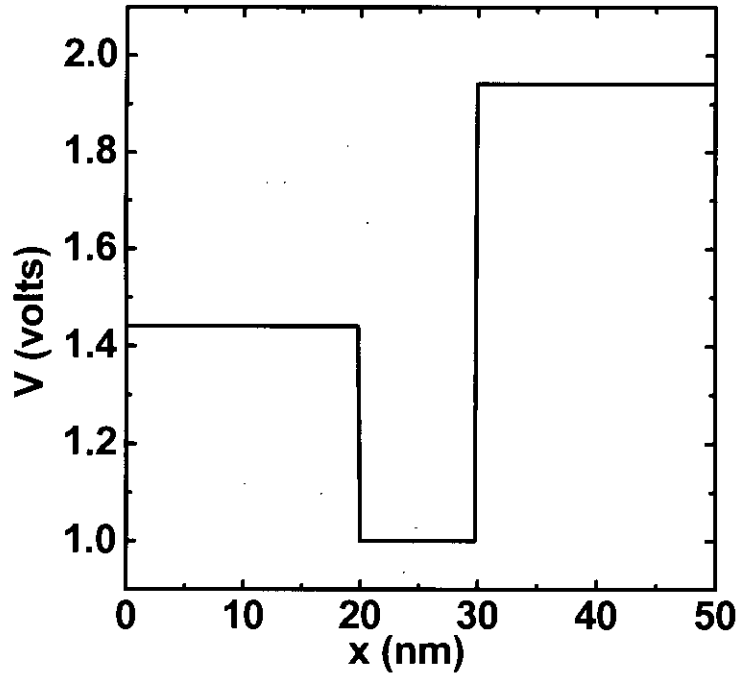


Figure 2.4: The initial guess of the potential distribution for $V_G = 0$.

assumed to have the same potential as the atom they belong to. When we get the converged potential profile, current is calculated from Equation 2.34.

2.7 Current Calculation Using Effective Mass Approximation

Instead of considering the atomic positions of the NW, we can visualize the nanowire having several grid points within the NW and obtain the Hamiltonian by discretizing the Schrodinger equation written in the cartesian co-ordinate. Hamiltonian thus formed can be used in the RGFA algorithm in the same way as the atomistic Hamiltonian was. But the dimension of the latter is much shorter and the computation time will be dramatically reduced. But the reliability will inevitably be reduced for small dimension NW when the atomistic approach will be the only option. Next we describe how the Schrodinger equation was discretized.

The Schrodinger equation in 3D cartesian coordinates is

$$-\frac{\hbar^2}{2} \left[\frac{\partial}{\partial x} \left(\frac{1}{m_x} \frac{\partial \psi}{\partial x} \right) + \frac{\partial}{\partial y} \left(\frac{1}{m_y} \frac{\partial \psi}{\partial y} \right) + \frac{\partial}{\partial z} \left(\frac{1}{m_z} \frac{\partial \psi}{\partial z} \right) \right] = E\psi \quad (2.49)$$

where ψ is the wave function, m_x , m_y , and m_z are the effective masses in device coordinates, and \hbar is the reduced Planck's constant. The nanowire is grown in $\langle 100 \rangle$ direction, which is device x coordinate in our study. Ballistic transport is assumed and recursive Green's function algorithm (RGFA) [25] is used to solve Schrodinger equation for charge density and current calculations. The open boundary condition in transport direction (x) is included in Schrodinger equation via self-energy matrices and hard-wall boundary condition is used in the transverse directions (y and z). The Schrodinger equation is discretized using finite difference method and it becomes

$$t_x \psi_{i+1,j,k} + t_x \psi_{i-1,j,k} + t_y \psi_{i,j+1,k} + t_y \psi_{i,j-1,k} + t_z \psi_{i,j,k+1} + t_z \psi_{i,j,k-1} - 2(t_x + t_y + t_z) \psi_{i,j,k} = E \psi_{i,j,k}$$

where,

$$\begin{aligned} t_x &= -\frac{\hbar^2}{2m_x(\Delta x)^2} \\ t_y &= -\frac{\hbar^2}{2m_y(\Delta y)^2} \\ t_z &= -\frac{\hbar^2}{2m_z(\Delta z)^2} \end{aligned} \quad (2.51)$$

Here Δx , Δy , Δz are the grid spacing in x , y and z direction respectively and $i = 1, 2, j = 1, 2, 3, \dots, N_y, k = 1, 2, 3, \dots, N_z$ where N_y and N_z are the number of grid points in y , and z direction respectively. For RGFA, the layer (cross-section) Hamiltonian and layer-to-layer coupling matrices are calculated from discretized Schrodinger equation. The left hand side of the Schrodinger equation can be represented in matrix form as

Chapter 3

Results and Discussions

3.1 Electronic Properties of Silicon Nanowire

The electronic properties, namely the band structure, the bandgap, and the electron effective masses of SiNWs are studied in this section. The SiNWs used in this study are grown in $\langle 100 \rangle$ and $\langle 110 \rangle$ directions. During nanowire growth, the bulk bond length is assumed and the dangling bonds are passivated with hydrogen atoms. The cross sections of $\langle 100 \rangle$ and $\langle 110 \rangle$ SiNWs are shown in Figure 3.1. The gray atoms are Silicon and the black atoms are hydrogen. The nanowire growth direction is x , which is into (or out of) the paper. The y and z directions are $\langle 010 \rangle$ and $\langle 001 \rangle$, respectively for the $\langle 100 \rangle$ wires, and $\langle \bar{1}10 \rangle$ and $\langle 001 \rangle$, respectively for the $\langle 110 \rangle$ wires. The cross section of $\langle 100 \rangle$ wire looks rectangular. The unit cell is 0.543 nm long and has 4 atomic layers. The $\langle 110 \rangle$ nanowire looks hexagonal. It has 2 atomic layers in a 0.384 nm unit cell.

The calculated band structure of $\langle 100 \rangle$ and $\langle 110 \rangle$ wires are shown in Figure 3.2 and 3.3, respectively. The cross section of $\langle 100 \rangle$ wire is 3.295 nm \times 3.295 nm, and that of $\langle 110 \rangle$ wire is 3.508 nm \times 3.508 nm. Both the wires show direct band gap. The bulk Silicon is an indirect band gap material with conduction band minima at $0.832 \times 2\pi/a$ in the Δ direction. The conduction band minima of bulk Silicon have six equivalent Δ valleys. For nanowire grown in $\langle 100 \rangle$ direction, four of the six equivalent Δ valleys (i.e., $[0 \pm 10]$ and $[00 \pm 1]$) are projected to

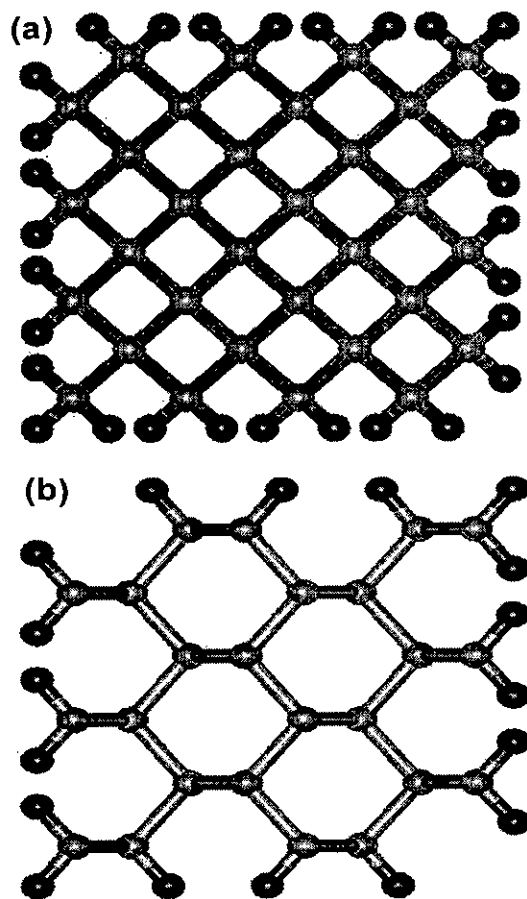


Figure 3.1: The cross sections of (a) $\langle 100 \rangle$ and (b) $\langle 110 \rangle$ nanowires. The gray atoms are Silicon and the black atoms are hydrogen.

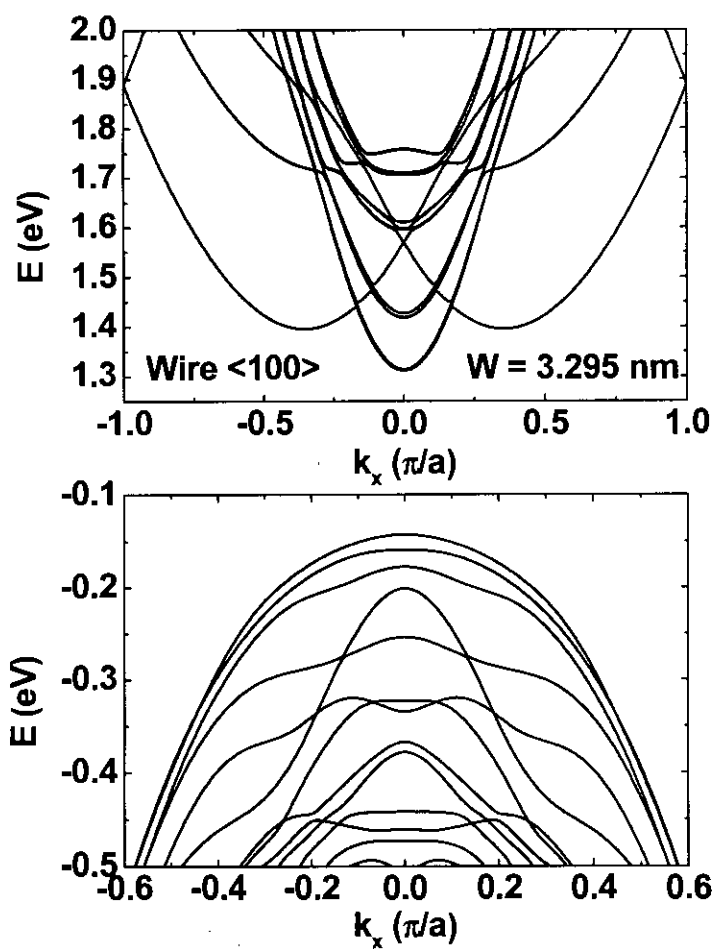


Figure 3.2: The band structure plots (E vs. k) of a $\langle 100 \rangle$ wire of cross section $3.295 \text{ nm} \times 3.295 \text{ nm}$.

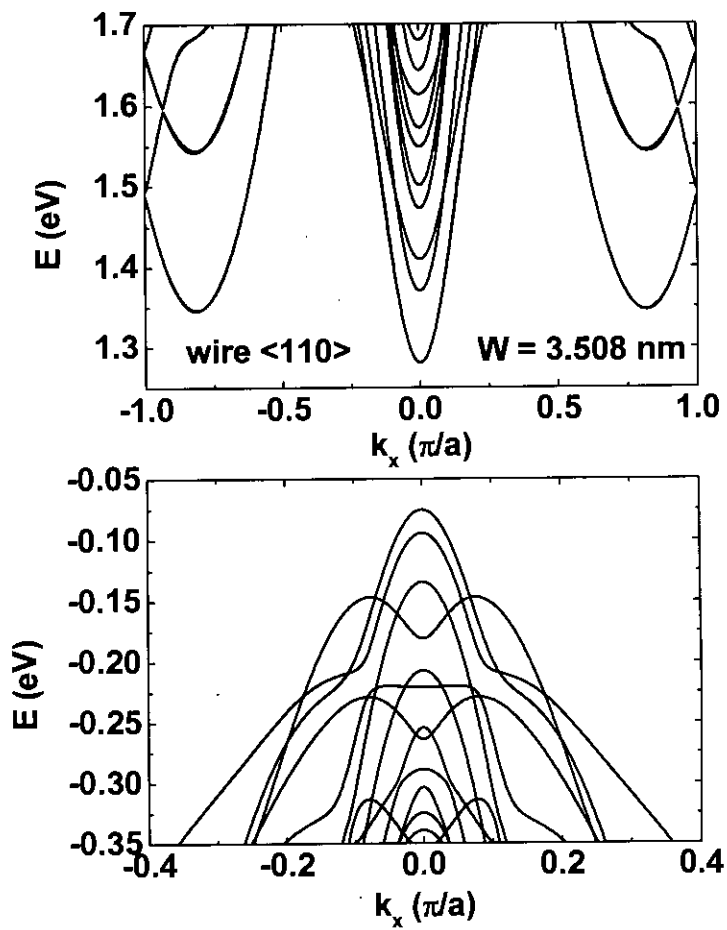


Figure 3.3: The band structure plots (E vs. k) of a $\langle 110 \rangle$ wire of cross section $3.508 \text{ nm} \times 3.508 \text{ nm}$.

the Γ point in the one dimensional Brilluoin zone to form the conduction band edge. The other two Δ valleys (i.e., $[\pm 100]$) are zone folded to the points $k_x = \pm 0.355 \times \pi/a$ in the wire Brilluoin zone. In Figure 3.2, we see that the four bands are degenerate at Γ point. However, they split due to quantization effects for NWs with smaller cross section, and this feature has been observed before (Figure 1(a) of Reference [8]). Two unprimed bulk valleys are projected at Γ point to form the conduction band edge in $\langle 110 \rangle$ wire as shown in Figure 3.3. The valley splitting at the conduction band minimum (Γ point) is not observed here. Our simulation shows that the valley splitting becomes significant for wire width < 2 nm (results are not shown here). This observation matches with the results reported in [13]. A second valley is observed at $k_x \approx 0.81\pi/a$, and the splitting between these two valleys is ≈ 65 meV. This splitting increases for smaller wire and the second valley slightly moves from $k_x \approx 0.81\pi/a$. Note that a is the unit cell length, and it is 0.543 nm for the $\langle 100 \rangle$ wires and 0.384 nm for the $\langle 110 \rangle$ wires.

The band gap E_g versus the wire dimension for both the $\langle 100 \rangle$ and $\langle 110 \rangle$ wires are shown in Figure 3.4.

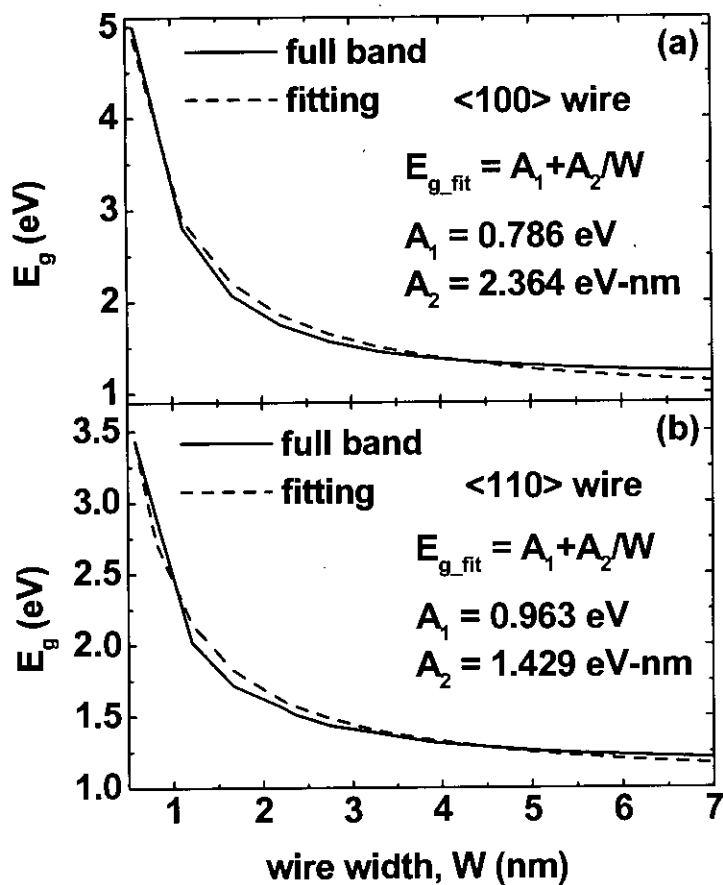


Figure 3.4: The band gap versus wire dimension for the (a) $\langle 100 \rangle$ and (b) $\langle 110 \rangle$ wires. The solid lines are calculated from the $sp^3d^5s^*$ orbital basis and the dashed lines are fitting to analytic expression.

The band gap falls rapidly with wire dimension for smaller cross sections and then slowly approaches the bulk value. At the same cross section, the $\langle 100 \rangle$ wire has larger band gap compared to the $\langle 110 \rangle$ wire. The band gap for both the wires are fitted to the analytic expression $A_1 + A_2/W$ and are shown as the dashed lines in Figure 3.4. Here W is the wire width in nanometer and the values of fitting parameters A_1 and A_2 are listed in the plots.

Next we parameterize the effective masses where the masses depend on the wire dimensions. The electron effective masses for unprimed valleys m_{Δ_4} at Γ point and for the primed valleys m_{Δ_2} at $k_x = 0.355 \times \pi/a$ for the $\langle 100 \rangle$ wires are shown in Figure 3.5 as a function of wire width. The effective mass is calculated from

$$\frac{1}{m^*} = \frac{1}{\hbar^2} \frac{\partial^2 E}{\partial k_x^2} = \frac{1}{\hbar^2} \frac{E_- - 2E_0 + E_+}{(\Delta k_x)^2}, \quad (3.1)$$

where E_0 is the energy at the bottom of a conduction band valley and E_+ and E_- are the energies at $\pm \Delta k_x$ from the valley, respectively. We use a Δk_x value of $(0.005) \times \pi/a$ for effective mass calculation. Note that the bulk effective masses calculated by Boykin [24], from where the energy integral values are taken, uses a modified k-p method and incomplete eigen state basis. The modified k-p method and the text book formula (Equation 3.1), however, have excellent agreement [31], and we, therefore, use the textbook formula for simplicity. The curvature of band at the valleys increases with wire width, and therefore, the effective masses, m_{Δ_4} and m_{Δ_2} , decrease with wire width and approach the bulk values of $0.201m_0$ and $0.89m_0$ [24], respectively. The effective mass values at Γ point, m_{Δ_4} , match with published values, Figure 3(b) of [13], Figure 2 of [17], Figure 5(a) of [12], and Figure 8(b) of [16]. However, our m_{Δ_4} is numerically larger compared to the m_{Δ_4} calculated for $\langle 001 \rangle$ wires by Zheng *et al.*, Figure 6(a) of [11]. For example, m_{Δ_4} is $\approx 0.376m_0$ for 2 nm wire in our calculation, and this value is $\approx 0.3m_0$ for 2 nm wire in [11]. In our simulation results (not shown here), we notice that the Δ_2 valley does not appear for nanowires of smaller dimension. This observation

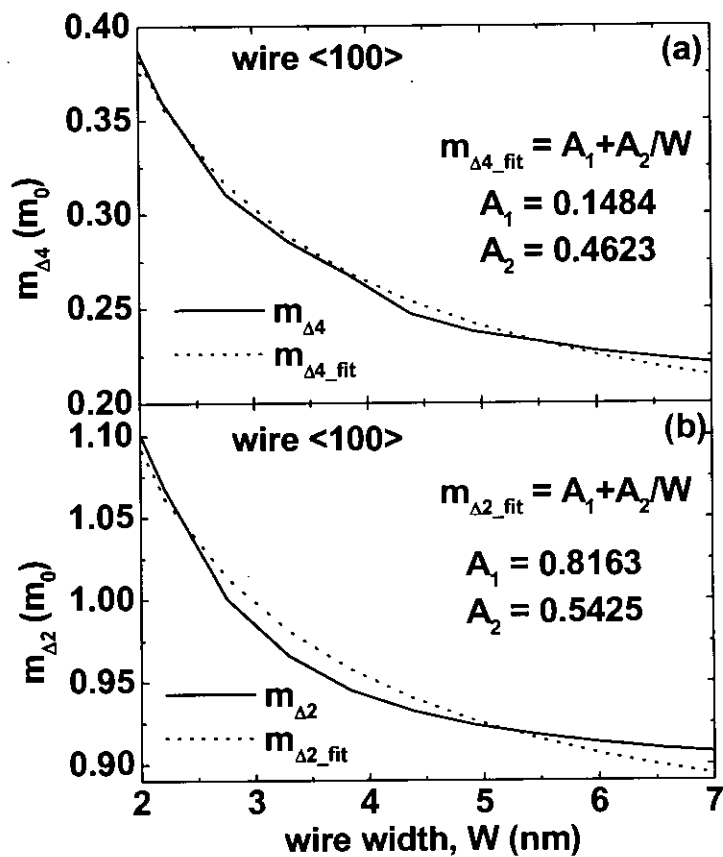


Figure 3.5: The electron effective masses $m_{\Delta 4}$ and $m_{\Delta 2}$ versus wire dimension for the $\langle 100 \rangle$ wires. The solid lines are calculated from the $sp^3d^5s^*$ orbital basis and the dotted lines are fitting to analytic expression.

matches with Figure 1(a) of [8], Figure 2(a) of [16], and Figure 3(a) of [12]. We fitted the effective masses, $m_{\Delta 4}$ and $m_{\Delta 2}$, to the analytic expression $A_1 + A_2/W$, where W is the wire width in nm. The fitted values are shown in Figure 3.5 as the dotted lines. The fitting parameters are $A_1 = 0.1484$ and $A_2 = 0.4623 \text{ nm}^{-1}$ for $m_{\Delta 4}$ and $A_1 = 0.8163$ and $A_2 = 0.5425 \text{ nm}^{-1}$ for $m_{\Delta 2}$, respectively.

The effective masses for $\langle 110 \rangle$ wire are shown in Figure 3.6. Here m_1 is the effective mass at the Γ point of the 1D Brillouin zone of the nanowire and m_2 is the effective mass at the second valley as shown in the band structure plots of Figure 3.3 at $k_x = 0.81\pi/a$. m_2 decreases with wire width and approaches the bulk value as $m_{\Delta 4}$ and $m_{\Delta 2}$ of $\langle 100 \rangle$ wire. However, m_1 increases with wire width and approaches the bulk value. The increase of m_1 with wire width can be understood from the E-k plots as shown in Figure 3.6(c). The plots are the E-k near Γ point for two different wire widths. Note that the bottoms of the conduction bands for the two wires are not at the same energy. They have been shifted for comparison. From the E-k plots, we see that the curvature of the conduction band near the Γ point of the $\langle 110 \rangle$ wire decreases with wire width that results in increase in the effective mass (see Equation (3.1)). The masses are also fitted to the analytic expression $m^* = A_1 + A_2/W$ and are shown in Figure 3.6 (a) and (b) as the dotted lines. The values of A_1 and A_2 are also listed there.

3.2 Effects of Cross-Sectional Shape on the Electronic Properties

Figure 3.7 shows the bandstructure for three different cross-sectional shapes while keeping the cross-section area same at 2.65 nm^2 . Figure 3.8(a) shows the variation of band gap with dimension. The band gap increases with decreasing cross-section area as a result of quantum confinement. For large wires, the bandgap equals that of bulk Silicon (1.13eV). When plotted against dimension, square nanowires exhibit lowest bandgaps and the bandgap for the triangular wire is the highest. But

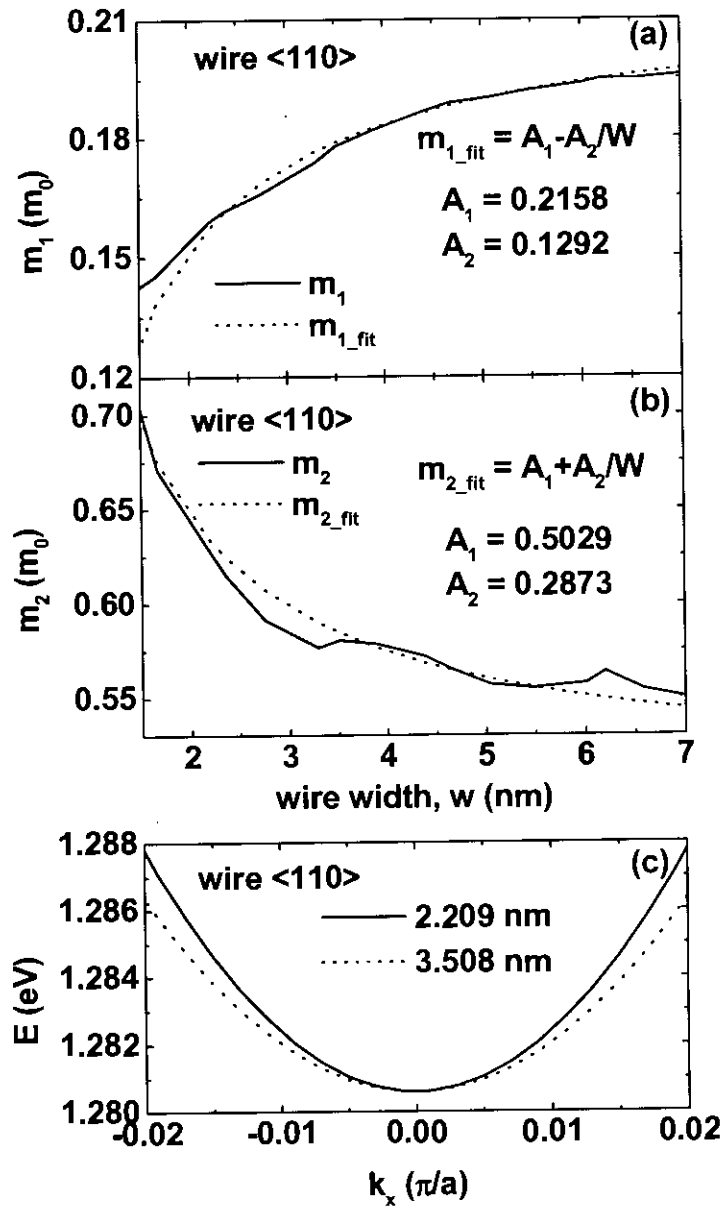


Figure 3.6: The electron effective masses m_1 and m_2 versus wire dimension for the $\langle 110 \rangle$ wires. The definitions of m_1 and m_2 are given in the text. The solid lines are calculated from the $sp^3d^5s^*$ orbital basis and the dotted lines are fitting to analytic expression. Figure (c) is the E-k relations near the Γ point for two different wires to explain the behavior of m_1 with wire dimension.

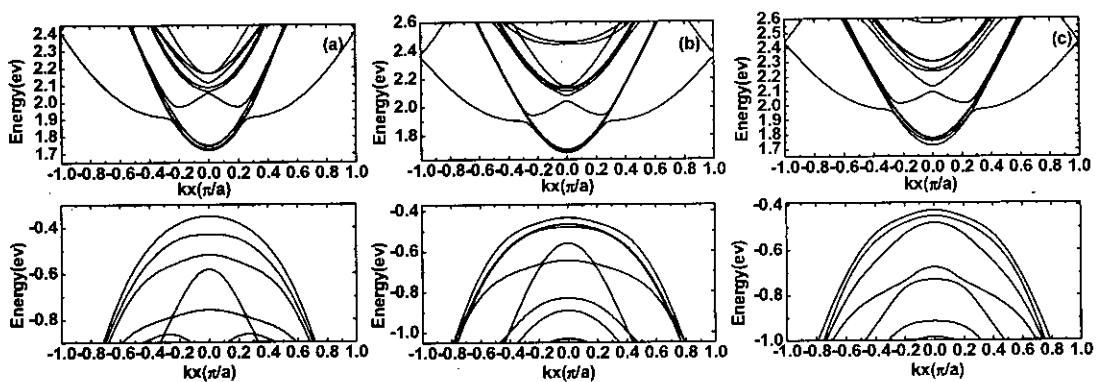


Figure 3.7: The bandstructure of $\langle 100 \rangle$ SiNWs with (a) square, (b) Circular, (c) Triangular cross-section

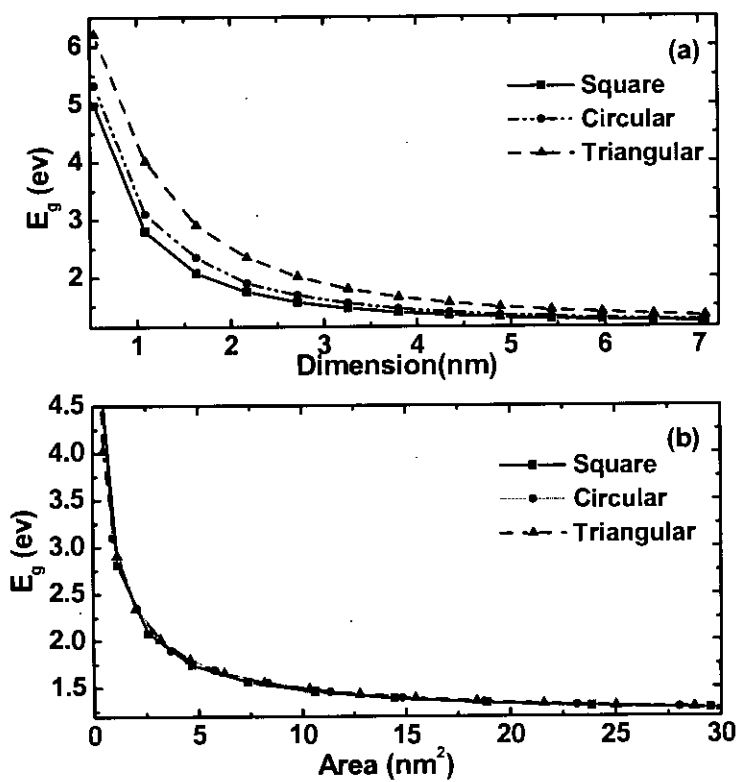


Figure 3.8: Bandgap variation with (a) dimension, (b) cross-section area.

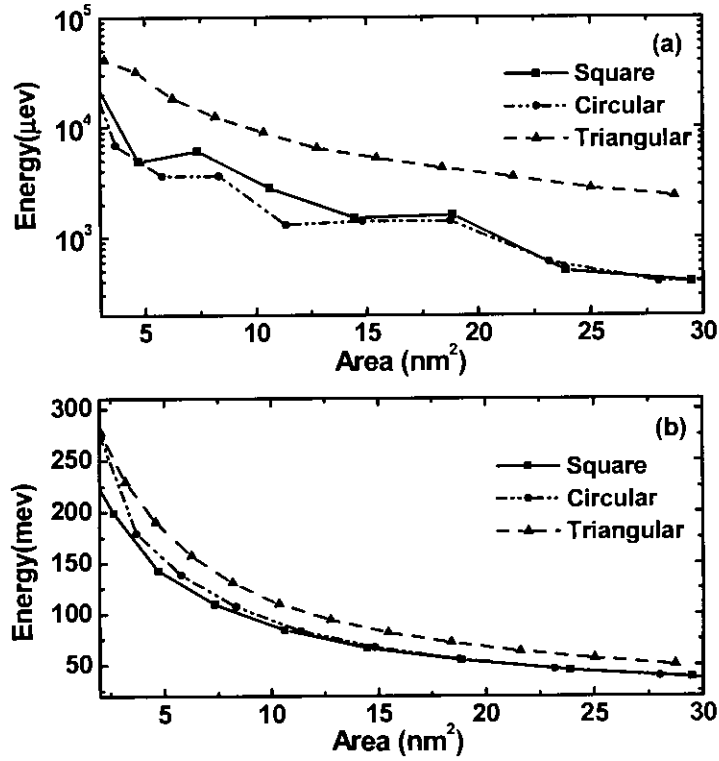


Figure 3.9: Effect of wire cross-section area on Δ_4 and Δ_2 conduction band valleys, (a) Variation of fourth highest conduction band energy at Δ_4 valley taking the lowest energy as reference, (b) Splitting of Δ_4 and Δ_2 valleys.

this dissimilarity is not for wire shape, because the triangular wire with dimension D has an area of $0.433D^2$, which is 43.3% of the square wire area (D^2) having the same dimension D . This fact is clear when we plot the bandgap against cross-section area, the bandgap for all shapes are remarkably similar (Figure 3.8 (b)). This reveals that the energy gap simply depends on the wire cross-section area, not on the shape.

The conduction band degeneracy at the Γ point for $\langle 100 \rangle$ wire is considered next (Figure 3.9 (a)). The fourth highest band is plotted taking the lowest conduction band as reference. The four valley degeneracy is almost similar for square and circular wires, while the valleys are less degenerate for triangular wire. As the

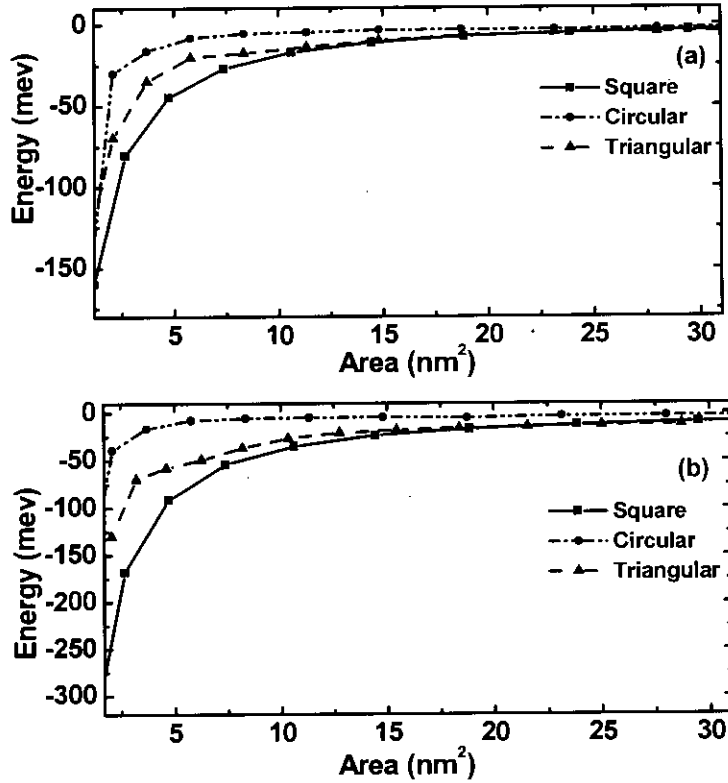


Figure 3.10: Effect of wire area on the splitting of the three highest valence bands taking the highest valence band Ev_1 as reference, (a) The energies Ev_2 and (b) Ev_3 with respect to Ev_1 .

cross-section area is increased, the separation between Δ_4 and Δ_2 valley energies is decreased (Figure 3.9 (b)). This energy difference is lowest for square wire and highest for triangular wire. Figure 3.10 shows the effect of quantum confinement on the three highest valence bands. The second and third highest valence bands are plotted taking the topmost valence band as reference. Here the valence band splitting is lowest for circular wire. Splitting for triangular wire is less than that of square wire at lower area ($< 12.0 \text{ nm}^2$) after which it is similar for both the wires.

Next we calculate effective masses at Δ_4 and Δ_2 valleys for $\langle 100 \rangle$ oriented nanowires. The effective mass at Δ_4 valley decreases with wire area and approaches the bulk Si transverse electron effective mass of $0.20 \cdot m_0$ as area is in-

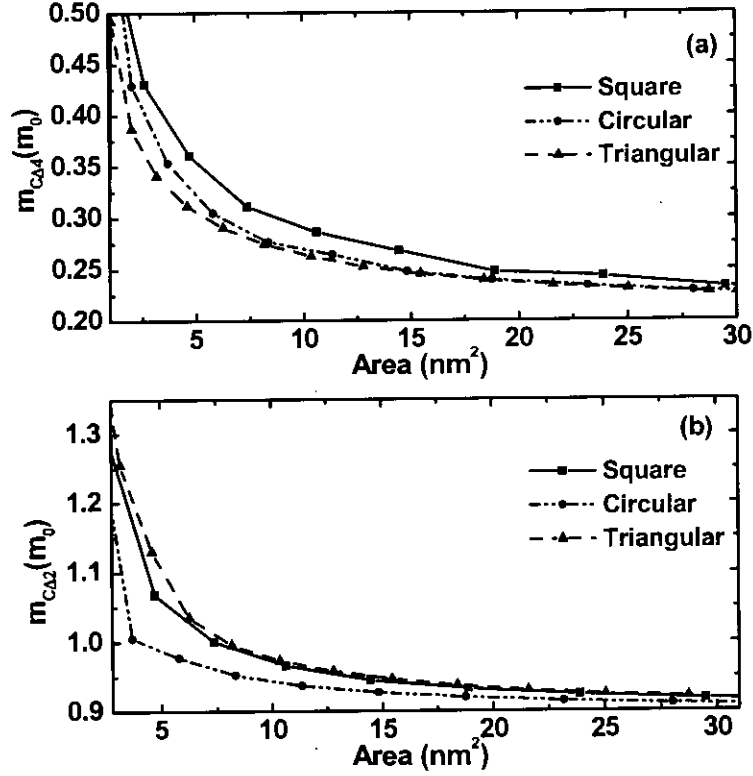


Figure 3.11: Electron effective mass for $\langle 100 \rangle$ wire at (a) Δ_4 valley (b) Δ_2 valley versus area.

creased as shown in Figure 3.11. At Δ_4 valley effective mass is highest for square wire and that of triangular wire is the lowest. m_c^* at Δ_2 valley is lowest for circular wire while that of the other two are almost similar. m_c^* at Δ_2 valley reaches the bulk Si longitudinal electron effective mass of $0.89m_0^*$ for large wires ($>6\text{nm}$). Electron effective mass at the Γ point for $\langle 110 \rangle$ wire m_1 is shown in Figure 3.12 (a). With dimension, m_1 increases until it reaches the bulk value (0.20^*m_0). Again the triangular wires show lower values than the other two wires. Figure 3.12 (b) shows the electron effective mass m_2 at $\pm 0.81 \times \pi/a$. It decreases with wire area and reaches a steady value of 0.55^*m_0 for large wires. Then we calculate hole effective mass for the highest valence band for $\langle 100 \rangle$ wire. Figure 3.13 shows the variation of hole effective mass. For triangular wire, hole effective mass is

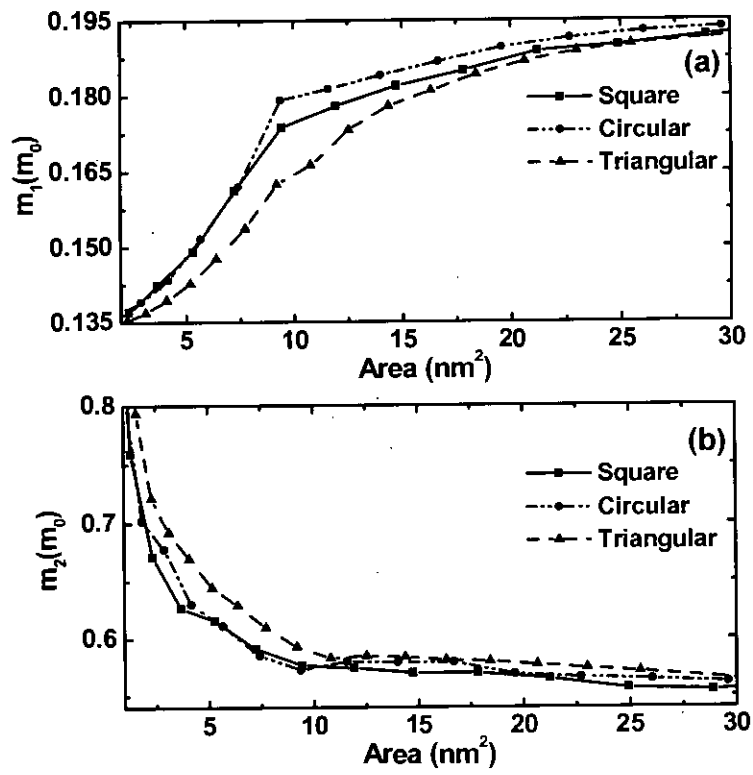


Figure 3.12: Variation of electron effective mass with area for <110> wire, (a) m_1 and (b) m_2 . The definitions of m_1 and m_2 are given in the text.

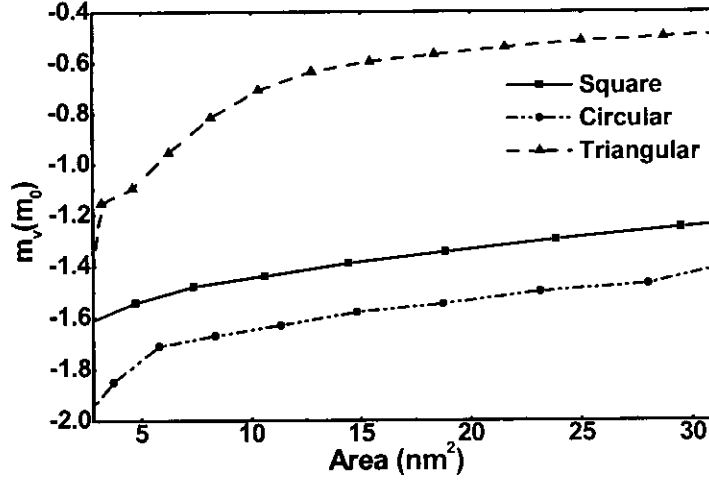


Figure 3.13: Variation of hole effective mass with area for $\langle 100 \rangle$ wire.

approximately two times larger than that of the bulk Si heavy hole at large dimension. It reaches a value of $-0.5m_0^*$ for cross-section area $> 20nm^2$. For square and circular wires, hole effective masses are much heavier (atleast five time than the bulk value). m_v^* is highest (magnitude only) for circular wire. For reference, the bulk Si valence band $\langle 100 \rangle$ effective mass is $m_{hh} = -0.276m_0$.

3.3 I-V Response of the SiNWFET

In this section we calculate the current-voltage characteristics of a SiNWFET using $sp^3d^5s^*$ orbital basis with $\langle 110 \rangle$ wire as the channel material. We next evaluate the performance metrics of the transistor and compare the full band current-voltage characteristics with the I-V calculated from the parameterized nanowire effective mass Hamiltonian.

The simulated full band ($sp^3d^5s^*$ orbital basis) I_D versus V_{GS} characteristics are shown in Figure 3.14, both in log and linear scales. The drain voltage is 0.5 V and the gate bias ranges from 0.0 V to 0.5 V. The device has a threshold voltage of ≈ 0.3 V and the on/off current ratio of 1.8×10^7 . The inverse subthreshold slope is ≈ 60 mV/dec.

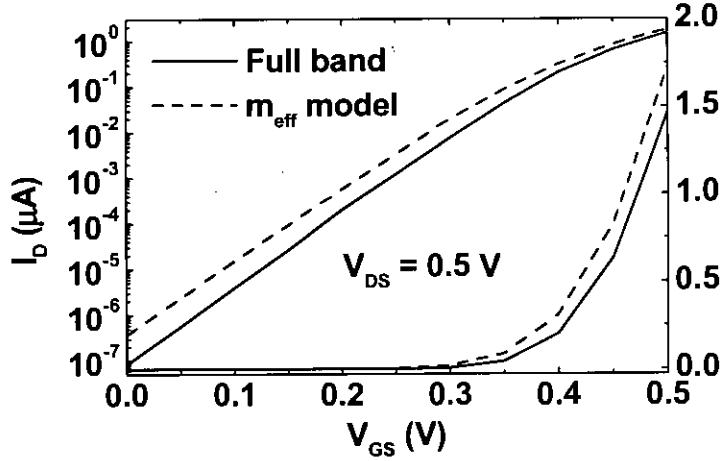


Figure 3.14: Simulated I_D versus V_{GS} plots. The solid lines are full band calculation and the dashed lines are calculated from nanowire confined effective mass model. The nanowire is $\langle 110 \rangle$ with cross section of $0.82 \text{ nm} \times 0.82 \text{ nm}$.

To understand the transport physics, we plot, in Figure 3.15, the energy band diagrams in both off ($V_{GS} = 0.0 \text{ V}$ & $V_{DS} = 0.5 \text{ V}$) and on ($V_{GS} = 0.5 \text{ V}$ & $V_{DS} = 0.5 \text{ V}$) states superimposed on the energy distribution of current. The source Fermi level is at 0.0 eV and the drain Fermi level is set to -0.5 eV . Note that the valence bands are not shown because the current through the valence bands is zero. The current has both the tunneling and the thermal components. The thermal component of the current can be evaluated by integrating J from the top of the conduction band to ∞ , and the tunneling component can be evaluated by integrating J from $-\infty$ to the top of the conduction band. The off state current has about 38% tunneling and 62% thermal currents and the on state current has about 50% tunneling and 50% thermal components. We observe that the current density, J , has a peak at an energy slightly below the top of the conduction band in the on state and slightly above the top of the conduction band in the off state.

Next we numerically calculate the figures of merit, namely the gate capacitance C_g , the transconductance g_m , the intrinsic switching delay τ_S , and the unity current gain frequency f_T . The gate capacitance is calculated from the electric

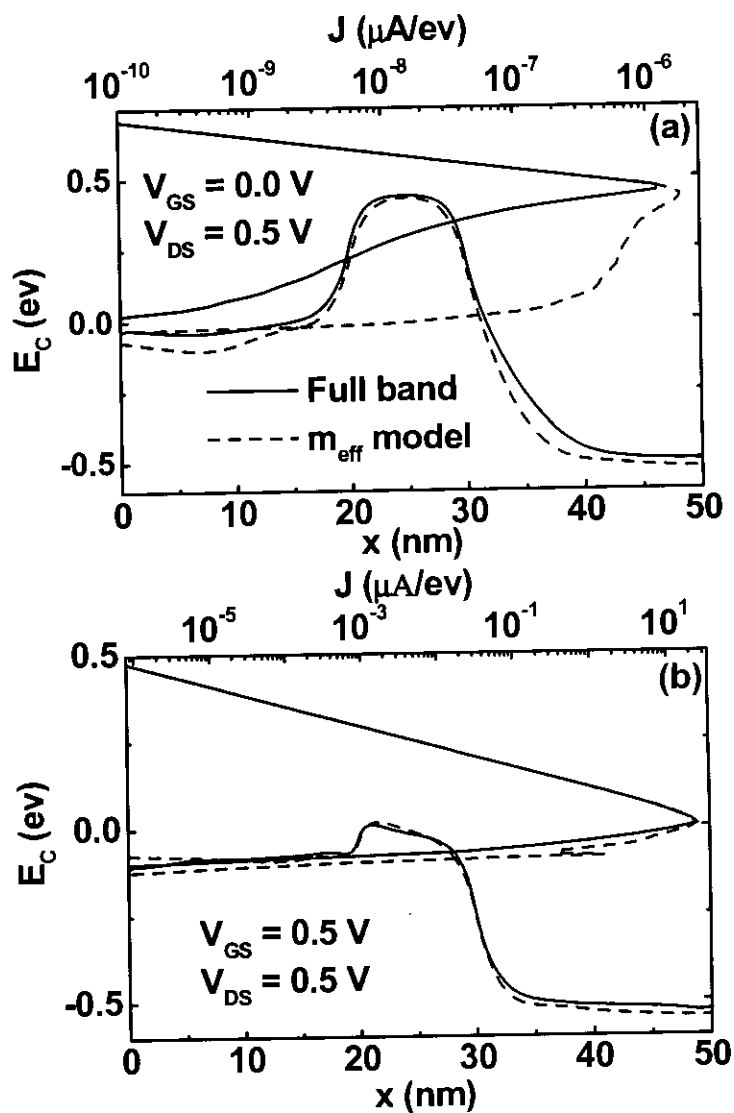


Figure 3.15: The conduction bands superimposed on the energy distribution of current in both (a) off-state and (b) on-state. The solid lines are full band calculation and the dashed lines are calculated from nanowire confined effective mass model.

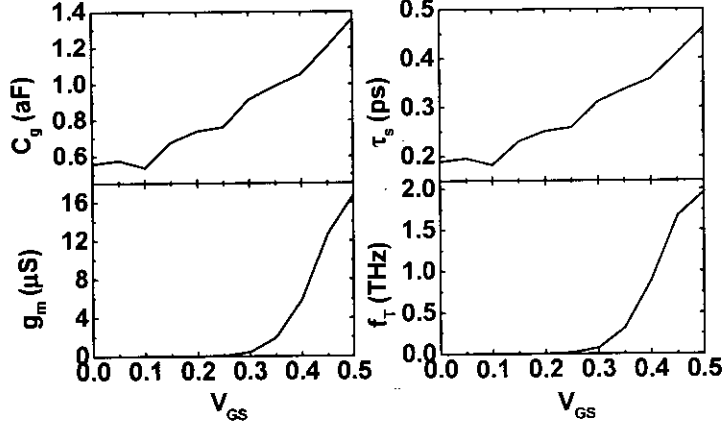


Figure 3.16: The gate capacitance, the transconductance, the switching delay, and the unity current gain frequency versus gate bias. The drain to source bias is fixed to 0.5 V.

flux density vector normal to the gate metal surface

$$C_g = 2\pi R \int_0^{L_g} dz \frac{\delta D_r}{\delta V_g} + 2\pi \int_{t_{ox}}^{t_{ox}-ex} r dr \frac{\delta D_z}{\delta V_g}. \quad (3.2)$$

The first integral is over the length of the gate along the bottom of the gate metal. The second integral is over the two sides of the gate metal. Equation (3.2) gives the total gate capacitance, $C_g = C_{gs} + C_{gd}$ which includes the effect of the quantum capacitance and the fringing fields directly from the gate metal to the source and drain. The transconductance g_m is calculated from $g_m = \partial I_D / \partial V_{GS}$, the intrinsic gate delay τ_S from $\tau_S = C_g V_{DD} / I_{ON}$, and the intrinsic unity current gain frequency f_T from $f_T = g_m / 2\pi C_g$. Here V_{DD} is 0.5 V in our study and I_{ON} is the on state current.

The gate capacitance, the transconductance, the intrinsic switching delay, and the intrinsic unity current gain frequency are shown in Figure 3.16. The gate capacitance is very small in the atto Farad range due to low gate dielectric SiO_2 . The switching delay is in the fraction of picosecond and the intrinsic unity current gain frequency is in tera Hertz. The on state transconductance value is $\approx 18 \mu\text{S}$.

Finally we self-consistently calculate the I-V using the effective masses ex-

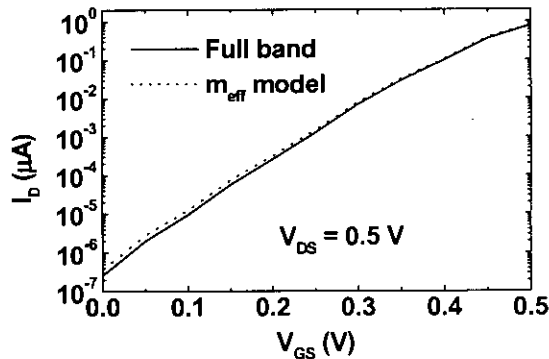


Figure 3.17: Simulated I_D versus V_{GS} plots. The solid lines are full band calculation and the dotted lines are calculated from nanowire confined effective mass model. The nanowire is $\langle 110 \rangle$ with cross section of $1.2 \text{ nm} \times 1.2 \text{ nm}$.

tracted from the band structure. The simulated current is shown in Figure 3.14 as the dashed lines in both log and linear scales. The effective mass model overestimates the current. This overestimation is larger in the off state and almost negligible in the on state. The reason can be explained from the band profiles superimposed on the energy distribution of current as shown in Figure 3.15 as the dashed lines. The thermal current is same, however, the tunneling current is overestimated by the nanowire confined effective mass model and this overestimation is larger in off state. This is because the tunnel barrier shape is almost similar for both the full band and the nanowire effective mass models in the on-state. The mismatch in the calculated I-V from the full band and nanowire effective mass models is noticeable for this small wire $0.82 \text{ nm} \times 0.82 \text{ nm}$. This mismatch is expected to improve for relatively thicker wires. This is indeed the case. The simulated full band and nanowire effective mass I-V characteristics for $1.2 \text{ nm} \times 1.2 \text{ nm}$ wire are shown in Figure 3.17. The calculated I-V characteristics show very good agreement. The full band and nanowire effective mass models comparison is not performed for wires $> 1.2 \text{ nm}$ due to computational resource limitation. The reason that the nanowire effective mass model shows excellent agreement with full band calculations for wire width down to 1.2 nm can also be explained from a

different viewpoint. The electron transport usually involves in the lowest 2 to 3 energy subbands, and the lowest three energy subbands calculated from nanowire effective masses and $sp^3d^5s^*$ atomic orbital basis match exactly for wire width down to 1.5 nm [32].

Chapter 4

Conclusions

Electronic properties of Silicon nanowires are observed for different crystal orientation, cross-sectional size and shape using nearest neighbor $sp^3d^5s^*$ atomic orbital basis with empirical tight binding parameters. Band gap and effective mass show strong variations as a result of quantum confinement and they also vary with crystal orientation. Cross-sectional shape has its effect on effective mass and triangular wires have the lowest effective mass compared with the other shapes. Then full band simulation of a Silicon nanowire field effect transistor is performed using the same basis and the performance metrics is evaluated. The current is also calculated self-consistently from the nanowire confined effective mass model and is compared to full band calculation. The effective mass calculation is reasonably accurate for nanowire with >1.2 . The thermal component of current is same, however, the tunneling current is overestimated by the effective mass model for smaller dimension. The nanowire effective mass model is facilitated by calculating the band gap and electron effective masses using $sp^3d^5s^*$ atomic orbital basis and by fitting them to analytic expression.

4.1 Suggestions for Future Work

Calculating the I-V response from the full band hamiltonian requires significant amount of time. An efficient algorithm which will both be computationally efficient

and reliable even at lower dimensions is thus required. It can be achieved by combining both effective mass and atomistic approach.

Strain engineering has been one of the most useful techniques to improve device performance for conventional MOSFETs. For NWs too, strain can be used to modify the band gap and effective mass of the material and thus device performance can be enhanced. A comprehensive treatment of strain on NWs and the resulted device performance is still missing in the literature.

References

- [1] Y. Cui, Z. Zhong, D. Wang, W. U. Wang, and C. M. Lieber, "High performance silicon nanowire field effect transistors," *Nano Lett.*, vol. 3, no. 2, pp. 149–152, 2003.
- [2] H. C. Lin and C. J. Su, "High performance poly-Si nanowire NMOS transistors," *IEEE Trans. Nanotechnol.*, vol. 6, no. 2, pp. 206–212, 2007.
- [3] N. Singh, A. Agarwal, L. K. Bera, T. Y. Liow, R. Yang, S. C. Rustagi, C. H. Tung, R. Kumar, G. Q. Lo, N. Balasubramanian, and D.-L. Kwong, "High-performance fully depleted silicon nanowire (diameter ≤ 5 nm) gate-all-around CMOS devices," *IEEE Electron Dev. Lett.*, vol. 27, no. 5, pp. 383–386, 2006.
- [4] H. S. P. Wong, "Beyond the conventional transistor," *Solid State Electron.*, vol. 49, pp. 755–762, 2005.
- [5] S. M. Koo, M. D. Edelstein, Q. Li, C. A. Richter, and E. M. Vogel, "Silicon nanowires as enhancement-mode Schottky barrier field-effect transistors," *Nanotechnology*, vol. 16, pp. 1482–1485, 2005.
- [6] G. M. Cohen, M. J. Rooks, J. O. Chu, S. E. Laux, P. M. Solomon, J. A. Ott, R. J. Miller, and W. Haensch, "Nanowire metal-oxide-semiconductor field effect transistor with doped epitaxial contacts for source and drain," *Appl. Phys. Lett.*, vol. 90, no. 23, p. 233110, 2007.

- [7] Y. Wu, Y. Cui, L. Huynh, C. J. Barrelet, D. C. Bell, and C. M. Lieber, "Controlled growth and structures of molecular-scale silicon nanowires," *Nano Lett.*, vol. 4, no. 3, pp. 433–436, 2004.
- [8] J. Wang, A. Rahman, A. Ghosh, G. Klimeck, and M. Lundstrom, "Performance evaluation of ballistic silicon nanowire transistors with atomic-basis dispersion relations," *Appl. Phys. Lett.*, vol. 86, p. 093113, 2005.
- [9] Y. Huang, X. Duan, Y. Cui, L. J. Lauhon, K. H. Kim, and C. M. Lieber, "Logic gates and computation from assembled nanowire building blocks," *Science*, vol. 294, pp. 1313–1317, 2001.
- [10] Y. Cui, Q. Wei, H. Park, and C. M. Lieber, "Nanowire nanosensors for highly sensitive and selective detection of biological and chemical species," *Science*, vol. 293, pp. 1289–1292, 2001.
- [11] Y. Zheng, C. Rivas, R. Lake, K. Alam, T. B. Boykin, and G. Klimeck, "Electronic properties of silicon nanowires," *IEEE Trans. Electron Dev.*, vol. 52, no. 6, pp. 1097–1103, 2005.
- [12] K. Nehari, N. Cavassilas, J. L. Autran, M. Bescond, D. Munteanu, and M. Lannoo, "Influence of band-structure on electron ballistic transport in silicon nanowire MOSFETs: an atomistic study," in *Proceedings of ESSDERC*, Grenoble, France, 2005, pp. 229 – 232.
- [13] J. Wang, A. Rahman, G. Klimeck, and M. Lundstorm, "Bandstructure and orientation effects in ballistic Si and Ge nanowire FETs," in *Proceedings of the IEDM*. New York: IEEE, 2005, pp. 530–533.
- [14] Y. Ko, M. Shin, S. Lee, and K. W. Park, "Effects of atomistic defects on coherent electron transmission in Si nanowires: full band calculations," *J. Appl. Phys.*, vol. 89, no. 1, pp. 374–379, 2001.

- [15] M. Luisier, A. Schenk, W. Fichtner, and G. Klimeck, "Atomistic simulation of nanowires in the $sp^3d^5s^*$ tight-binding formalism: from boundary conditions to strain calculations," *Phys. Rev. B*, vol. 74, no. 20, p. 205323, 2006.
- [16] J. Wang, A. Rahman, A. Ghosh, G. Klimeck, and M. Lundstrom, "On the validity of the parabolic effective-mass approximation for the I-V calculation of silicon nanowire transistors," *IEEE Trans. Electron Dev.*, vol. 52, no. 7, pp. 1589–1595, 2005.
- [17] K. Nehari, N. Cavassilas, F. Michelini, M. Bescond, J. L. Autran, and M. Lannoo, "Full-band study of current across silicon nanowire transistors," *Appl. Phys. Lett.*, vol. 90, p. 132112, 2007.
- [18] E. Gnani, S. Reggiani, A. Gnudi, P. Parruccini, R. Colle, M. Rudan, and G. Baccarani, "Band-structure effects in ultrascaled silicon nanowires," *IEEE Trans. Electron Dev.*, vol. 54, no. 9, pp. 2243–2254, 2007.
- [19] M. Luisier, A. Schenk, and W. Fichtner, "Three-dimensional full-band simulations of Si nanowire transistors," *IEDM Tech. Dig.*, pp. 811–815, 2006.
- [20] —, "Atomistic treatment of interface roughness in Si nanowire transistors with different channel orientations," *Appl. Phys. Lett.*, vol. 90, no. 10, p. 102103, 2007.
- [21] T. B. Boykin, M. Luisier, and G. Klimeck, "Multiband transmission calculations for nanowires using an optimized renormalization method," *Phys. Rev. B*, vol. 77, p. 165318, 2008.
- [22] P. Marconcini, G. Fiori, M. Macucci, and G. Iannaccone, "Hierarchical simulation of transport in silicon nanowire transistors," *J. Comput. Electron.*, vol. 7, no. 3, pp. 415–418, 2008.

- [23] J. C. Slater and G. F. Koster, "Simplified LCAO method for the periodic potential problem," *Phys. Rev.*, vol. 94, no. 6, pp. 1498–1524, 1954.
- [24] T. B. Boykin, G. Klimeck, and F. Oyafuso, "Valence band effective-mass expressions in the $sp^3d^5s^*$ empirical tight-binding model applied to a Si and Ge parametrization," *Phys. Rev. B*, vol. 69, p. 115201, 2004.
- [25] R. Lake, G. Klimeck, R. C. Bowen, and D. Jovanovic, "Single and multi-band modeling of quantum electron transport through layered semiconductor devices," *J. Appl. Phys.*, vol. 81, no. 12, pp. 7845–7869, 1997.
- [26] K. Alam and R. K. Lake, "Leakage and performance of zero-schottky-barrier carbon nanotube transistors," *J. Appl. Phys.*, vol. 98, p. 064307, 2005.
- [27] S. Datta, *Quantum Transport Atom to Transistor*. Cambridge: Cambridge University Press, 2005.
- [28] M. Galperin, S. Toledo, and A. Nitzan, "Numerical computation of tunneling fluxes," *J. Chem. Phys.*, vol. 117, pp. 10 817–10 826, 2002.
- [29] E. Gnani, S. Reggiani, M. Rudan, and G. Bacarani, "Effects of high-K (HfO_2) gate dielectrics in double-gate and cylindrical-nanowire FETs scaled to the ultimate technology nodes," *IEEE Trans. Nanotechnol.*, vol. 6, pp. 90–96, 2007.
- [30] V. Eyert, "A comparative study on methods for convergence acceleration of iterative vector sequences," *J. Comput. Phys.*, vol. 124, no. 0059, pp. 271–285, 1996.
- [31] T. B. Boykin, "Incorporation of incompleteness in the k-p perturbation theory," *Phys. Rev. B*, vol. 52, pp. 16 317–16 320, 1995.

- [32] A. Martinez, M. Bescond, J. R. Barker, A. Svizhenko, M. P. Anantram, C. Millar, and A. Asenov, "A self-consistent full 3-d real-space NEGF simulation for studying nonperturbative effects in nano-MOSFETs," *IEEE Trans. Electron Dev.*, vol. 54, no. 9, pp. 2213–2222, 2007.

Appendix A

Energy Integrals for Crystal in terms of Two-Center Integrals¹

$$E_{s,s} = (ss\sigma)$$

$$E_{s,s^*} = (ss^*\sigma)$$

$$E_{s^*,s} = (s^*s\sigma)$$

$$E_{s,x} = l(sp\sigma)$$

$$E_{x,s} = (-1) \times l(sp\sigma)$$

$$E_{s,y} = m(sp\sigma)$$

$$E_{y,s} = (-1) \times m(sp\sigma)$$

$$E_{s,z} = n(sp\sigma)$$

$$E_{z,s} = (-1) \times n(sp\sigma)$$

$$E_{s,xy} = \sqrt{3}lm(sd\sigma)$$

$$E_{xy,s} = \sqrt{3}lm(sd\sigma)$$

$$E_{s,yz} = \sqrt{3}mn(sd\sigma)$$

$$E_{yz,s} = \sqrt{3}mn(sd\sigma)$$

$$E_{s,zx} = \sqrt{3}nl(sd\sigma)$$

$$E_{zx,s} = \sqrt{3}nl(sd\sigma)$$

$$E_{s,x^2-y^2} = \frac{1}{2}\sqrt{3}(l^2 - m^2)(sd\sigma)$$

$$E_{x^2-y^2,s} = \frac{1}{2}\sqrt{3}(l^2 - m^2)(sd\sigma)$$

$$E_{s,3x^2-r^2} = [n^2 - \frac{1}{2}(l^2 + m^2)](sd\sigma)$$

$$E_{3x^2-r^2,s} = [n^2 - \frac{1}{2}(l^2 + m^2)](sd\sigma)$$

¹A limited version is provided in Ref. [23] and the rest are derived.

$$E_{s^*,s^*} = (s^* s^* \sigma)$$

$$E_{s^*,x} = l(s^* p \sigma)$$

$$E_{x,s^*} = (-1) \times l(s^* p \sigma)$$

$$E_{s^*,y} = m(s^* p \sigma)$$

$$E_{y,s^*} = (-1) \times m(s^* p \sigma)$$

$$E_{s^*,z} = n(s^* p \sigma)$$

$$E_{z,s^*} = (-1) \times n(s^* p \sigma)$$

$$E_{s^*,xy} = \sqrt{3}lm(s^* d\sigma)$$

$$E_{xy,s^*} = \sqrt{3}lm(s^* d\sigma)$$

$$E_{s^*,yz} = \sqrt{3}mn(s^* d\sigma)$$

$$E_{yz,s^*} = \sqrt{3}mn(s^* d\sigma)$$

$$E_{s^*,zx} = \sqrt{3}nl(s^* d\sigma)$$

$$E_{zx,s^*} = \sqrt{3}nl(s^* d\sigma)$$

$$E_{s^*,x^2-y^2} = \frac{1}{2}\sqrt{3}(l^2 - m^2)(s^* d\sigma)$$

$$E_{x^2-y^2,s^*} = \frac{1}{2}\sqrt{3}(l^2 - m^2)(s^* d\sigma)$$

$$E_{s^*,3z^2-r^2} = [n^2 - \frac{1}{2}(l^2 + m^2)](s^* d\sigma)$$

$$E_{3z^2-r^2,s^*} = [n^2 - \frac{1}{2}(l^2 + m^2)](s^* d\sigma)$$

$$E_{x,x} = l^2(pp\sigma) + (1 - l^2)(pp\pi)$$

$$E_{x,y} = lm[(pp\sigma) - (pp\pi)]$$

$$E_{y,x} = lm[(pp\sigma) - (pp\pi)]$$

$$E_{x,z} = ln[(pp\sigma) - (pp\pi)]$$

$$E_{z,x} = ln[(pp\sigma) - (pp\pi)]$$

$$E_{x,xy} = \sqrt{3}l^2m(pd\sigma) + m(1 - 2l^2)(pd\pi)$$

$$E_{xy,x} = (-1) \times [\sqrt{3}l^2m(pd\sigma) + m(1 - 2l^2)(pd\pi)]$$

$$E_{x,yz} = \sqrt{3}lmn(pd\sigma) - 2lmn(pd\pi)$$

$$E_{yz,x} = (-1) \times [\sqrt{3}lmn(pd\sigma) - 2lmn(pd\pi)]$$

$$\begin{aligned}
E_{x,xx} &= \sqrt{3}l^2n(pd\sigma) + n(1 - 2l^2)(pd\pi) \\
E_{zx,x} &= (-1) \times [\sqrt{3}l^2n(pd\sigma) + n(1 - 2l^2)(pd\pi)] \\
E_{x,x2-y2} &= \frac{1}{2}\sqrt{3}l(l^2 - m^2)(pd\sigma) + l(1 - l^2 + m^2)(pd\pi) \\
E_{x2-y2,x} &= (-1) \times [\frac{1}{2}\sqrt{3}l(l^2 - m^2)(pd\sigma) + l(1 - l^2 + m^2)(pd\pi)] \\
E_{x,3z2-r2} &= l(n^2 - \frac{1}{2}(l^2 + m^2))(pd\sigma) - \sqrt{3}ln^2(pd\pi) \\
E_{3z2-r2,x} &= (-1) \times [l(n^2 - \frac{1}{2}(l^2 + m^2))(pd\sigma) - \sqrt{3}ln^2(pd\pi)]
\end{aligned}$$

$$\begin{aligned}
E_{y,y} &= m^2(pp\sigma) + (1 - m^2)(pp\pi) \\
E_{y,z} &= mn[(pp\sigma) - (pp\pi)] \\
E_{z,y} &= mn[(pp\sigma) - (pp\pi)] \\
E_{y,xy} &= \sqrt{3}lm^2(pd\sigma) + l(1 - 2m^2)(pd\pi) \\
E_{xy,y} &= (-1) \times [\sqrt{3}lm^2(pd\sigma) + l(1 - 2m^2)(pd\pi)] \\
E_{y,yz} &= \sqrt{3}m^2n(pd\sigma) + n(1 - 2m^2)(pd\pi) \\
E_{yz,y} &= (-1) \times [\sqrt{3}m^2n(pd\sigma) + n(1 - 2m^2)(pd\pi)] \\
E_{y,zx} &= \sqrt{3}lmn(pd\sigma) - 2lmn(pd\pi) \\
E_{zx,y} &= (-1) \times [\sqrt{3}lmn(pd\sigma) - 2lmn(pd\pi)] \\
E_{y,x2-y2} &= \frac{1}{2}\sqrt{3}m(l^2 - m^2)(pd\sigma) - m(1 + l^2 - m^2)(pd\pi) \\
E_{x2-y2,y} &= (-1) \times [\frac{1}{2}\sqrt{3}m(l^2 - m^2)(pd\sigma) - m(1 + l^2 - m^2)(pd\pi)] \\
E_{y,3z2-r2} &= m(n^2 - \frac{1}{2}(l^2 + m^2))(pd\sigma) - \sqrt{3}mn^2(pd\pi) \\
E_{3z2-r2,y} &= (-1) \times [m(n^2 - \frac{1}{2}(l^2 + m^2))(pd\sigma) - \sqrt{3}mn^2(pd\pi)]
\end{aligned}$$

$$\begin{aligned}
E_{z,z} &= n^2(pp\sigma) + (1 - n^2)(pp\pi) \\
E_{z,xy} &= \sqrt{3}lmn(pd\sigma) - 2lmn(pd\pi) \\
E_{xy,z} &= (-1) \times [\sqrt{3}lmn(pd\sigma) - 2lmn(pd\pi)] \\
E_{z,yz} &= \sqrt{3}n^2m(pd\sigma) + m(1 - 2n^2)(pd\pi) \\
E_{yz,z} &= (-1) \times [\sqrt{3}n^2m(pd\sigma) + m(1 - 2n^2)(pd\pi)] \\
E_{z,zx} &= \sqrt{3}n^2l(pd\sigma) + l(1 - 2n^2)(pd\pi) \\
E_{zx,z} &= (-1) \times [\sqrt{3}n^2l(pd\sigma) + l(1 - 2n^2)(pd\pi)]
\end{aligned}$$

$$\begin{aligned}
E_{z,x2-y2} &= \frac{1}{2}\sqrt{3}n(l^2 - m^2)(pd\sigma) - n(l^2 - m^2)(pd\pi) \\
E_{x2-y2,z} &= (-1) \times [\frac{1}{2}\sqrt{3}n(l^2 - m^2)(pd\sigma) - n(l^2 - m^2)(pd\pi)] \\
E_{z,3z2-r2} &= n(n^2 - \frac{1}{2}(l^2 + m^2))(pd\sigma) + \sqrt{3}n(l^2 + m^2)(pd\pi) \\
E_{3z2-r2,z} &= (-1) \times [n(n^2 - \frac{1}{2}(l^2 + m^2))(pd\sigma) + \sqrt{3}n(l^2 + m^2)(pd\pi)]
\end{aligned}$$

$$\begin{aligned}
E_{xy,xy} &= 3l^2m^2(dd\sigma) + (l^2 + m^2 - 4l^2m^2)(dd\pi) + (n^2 + l^2m^2)(dd\delta) \\
E_{xy,yz} &= 3lm2n(dd\sigma) + ln(1 - 4m^2)(dd\pi) + ln(m^2 - 1)(dd\delta) \\
E_{yz,xy} &= 3lm^2n(dd\sigma) + ln(1 - 4m^2)(dd\pi) + ln(m^2 - 1)(dd\delta) \\
E_{xy,zx} &= 3l^2mn(dd\sigma) + mn(1 - 4l^2)(dd\pi) + mn(l^2 - 1)(dd\delta) \\
E_{zx,xy} &= 3l^2mn(dd\sigma) + mn(1 - 4l^2)(dd\pi) + mn(l^2 - 1)(dd\delta) \\
E_{xy,x2-y2} &= \frac{3}{2}lm(l^2 - m^2)(dd\sigma) + 2lm(m^2 - l^2)(dd\pi) + \frac{1}{2}lm(l^2 - m^2)(dd\delta) \\
E_{x2-y2,xy} &= \frac{3}{2}lm(l^2 - m^2)(dd\sigma) + 2lm(m^2 - l^2)(dd\pi) + \frac{1}{2}lm(l^2 - m^2)(dd\delta) \\
E_{xy,3z2-r2} &= \sqrt{3}lm[n^2 - \frac{1}{2}(l^2 + m^2)](dd\sigma) - 2\sqrt{3}lmn^2(dd\pi) + \frac{1}{2}\sqrt{3}lm(1 + n^2)(dd\delta) \\
E_{3z2-r2,xy} &= \sqrt{3}lm[n^2 - \frac{1}{2}(l^2 + m^2)](dd\sigma) - 2\sqrt{3}lmn^2(dd\pi) + \frac{1}{2}\sqrt{3}lm(1 + n^2)(dd\delta)
\end{aligned}$$

$$\begin{aligned}
E_{yz,yz} &= 3n^2m^2(dd\sigma) + (n^2 + m^2 - 4n^2m^2)(dd\pi) + (l^2 + n^2m^2)(dd\delta) \\
E_{yz,zx} &= 3lmn^2(dd\sigma) + ml(1 - 4n^2)(dd\pi) + ml(n^2 - 1)(dd\delta) \\
E_{zx,yz} &= 3lmn^2(dd\sigma) + ml(1 - 4n^2)(dd\pi) + ml(n^2 - 1)(dd\delta) \\
E_{yz,x2-y2} &= \frac{3}{2}mn(l^2 - m^2)(dd\sigma) - mn[1 + 2(l^2 - m^2)](dd\pi) + mn[1 + \frac{1}{2}(l^2 - m^2)](dd\delta) \\
E_{x2-y2,yz} &= \frac{3}{2}mn(l^2 - m^2)(dd\sigma) - mn[1 + 2(l^2 - m^2)](dd\pi) + mn[1 + \frac{1}{2}(l^2 - m^2)](dd\delta) \\
E_{yz,3z2-r2} &= \sqrt{3}mn[n^2 - \frac{1}{2}(l^2 + m^2)](dd\sigma) + \sqrt{3}mn(l^2 + m^2 - n^2)(dd\pi) - \frac{1}{2}\sqrt{3}mn(l^2 + m^2)(dd\delta) \\
E_{3z2-r2,yz} &= \sqrt{3}mn[n^2 - \frac{1}{2}(l^2 + m^2)](dd\sigma) + \sqrt{3}mn(l^2 + m^2 - n^2)(dd\pi) - \frac{1}{2}\sqrt{3}mn(l^2 + m^2)(dd\delta)
\end{aligned}$$

$$\begin{aligned}
E_{zx,zx} &= 3n^2l^2(dd\sigma) + (n^2 + l^2 - 4n2l^2)(dd\pi) + (m^2 + n^2l^2)(dd\delta) \\
E_{zx,x2-y2} &= \frac{3}{2}nl(l^2 - m^2)(dd\sigma) + nl[1 - 2(l^2 - m^2)](dd\pi) - nl[1 - \frac{1}{2}(l^2 - m^2)](dd\delta) \\
E_{x2-y2,zx} &= \frac{3}{2}nl(l^2 - m^2)(dd\sigma) + nl[1 - 2(l^2 - m^2)](dd\pi) - nl[1 - \frac{1}{2}(l^2 - m^2)](dd\delta)
\end{aligned}$$

$$E_{zx,3z2-r2} = \sqrt{3}ln[n^2 - \frac{1}{2}(l^2 + m^2)](dd\sigma) + \sqrt{3}ln(l^2 + m^2 - n^2)(dd\pi) - \frac{1}{2}\sqrt{3}ln(l^2 + m^2)(dd\delta)$$

$$E_{3z2-r2,zz} = \sqrt{3}ln[n^2 - \frac{1}{2}(l^2 + m^2)](dd\sigma) + \sqrt{3}ln(l^2 + m^2 - n^2)(dd\pi) - \frac{1}{2}\sqrt{3}ln(l^2 + m^2)(dd\delta)$$

$$E_{x2-y2,x2-y2} = \frac{3}{4}(l^2 - m^2)^2(dd\sigma) + [l^2 + m^2 - (l^2 - m^2)^2](dd\pi) + [n^2 + \frac{1}{4}(l^2 - m^2)^2](dd\delta)$$

$$E_{x2-y2,3z2-r2} = \frac{1}{2}\sqrt{3}(l^2 - m^2)[n^2 - \frac{1}{2}(l^2 + m^2)](dd\sigma) + \sqrt{3}n^2(m^2 - l^2)(dd\pi) + \frac{1}{4}\sqrt{3}(1 + n^2)(l^2 - m^2)(dd\delta)$$

$$E_{3z2-r2,x2-y2} = \frac{1}{2}\sqrt{3}(l^2 - m^2)[n^2 - \frac{1}{2}(l^2 + m^2)](dd\sigma) + \sqrt{3}n^2(m^2 - l^2)(dd\pi) + \frac{1}{4}\sqrt{3}(1 + n^2)(l^2 - m^2)(dd\delta)$$

$$E_{3z2-r2,3z2-r2} = [n^2 - \frac{1}{2}(l^2 + m^2)]^2(dd\sigma) + 3n^2(l^2 + m^2)(dd\pi) + \frac{3}{4}(l^2 + m^2)^2(dd\delta)$$

Appendix B

Empirical Tight-Binding Parameters for Silicon (same-site and two-center integrals) in the Slater-Koster notation²

$$E_s = -2.15168$$

$$E_p = 4.22925$$

$$E_{s^*} = 19.11650$$

$$E_d = 13.78950$$

$$E_{ss\sigma} = -1.95933$$

$$E_{s^*s^*\sigma} = -4.24135$$

$$E_{ss^*\sigma} = -1.52230$$

$$E_{sp\sigma} = 3.02562$$

$$E_{s^*p\sigma} = 3.15565$$

$$E_{sd\sigma} = -2.28485$$

$$E_{s^*d\sigma} = -0.80993$$

$$E_{pp\sigma} = 4.10364$$

$$E_{pp\pi} = -1.51801$$

$$E_{pd\sigma} = -1.35554$$

$$E_{pd\pi} = 2.38479$$

$$E_{dd\sigma} = -1.68136$$

$$E_{dd\pi} = 2.58880$$

²Taken from [24]

$$E_{dd\delta} = -1.81400$$

$$E_{sh\delta\sigma} = -3.999720$$

$$E_{shs*\sigma} = -1.697700$$

$$E_{shp\sigma} = 4.251750$$

$$E_{shd\sigma} = -2.105520$$

Appendix C

Flow chart: The flow chart of the algorithm of self-consistent loop is shown in the next page.



